

Mixed-ADC Based PMCW MIMO Radar Angle-Doppler Imaging

Xiaolei Shang, Ronghao Lin and Yuanbo Cheng

Abstract—Phase-modulated continuous-wave (PMCW) multiple-input multiple-output (MIMO) radar systems are known to possess excellent mutual interference mitigation capabilities, but require costly and power-hungry high sampling rate and high-precision analog-to-digital converters (ADC's). To reduce cost and power consumption, we consider a mixed-ADC architecture, in which most receive antenna outputs are sampled by one-bit ADC's, and only one or a few outputs by high-precision ADC's. We first derive the Cramér-Rao bound (CRB) for the mixed-ADC based PMCW MIMO radar to characterize the best achievable performance of an unbiased target parameter estimator. The CRB analysis demonstrates that the mixed-ADC architecture with a relatively small number of high-precision ADC's and a large number of one-bit ADC's allows us to drastically reduce the hardware cost and power consumption while still maintain a high dynamic range needed for autonomous driving applications. We also introduce a two-step estimator to realize the computationally efficient maximum likelihood (ML) estimation of the target parameters. We formulate the angle-Doppler imaging problem as a sparse parameter estimation problem, and a computationally efficient majorization-minimization (MM) based estimator of sparse parameters, referred to as mLIKES, is devised for accurate angle-Doppler imaging. This is followed by using a relaxation-based approach to cyclically refine the results of mLIKES for accurate off-grid target parameter estimation. Numerical examples are provided to demonstrate the effectiveness of the proposed algorithms for angle-Doppler imaging using mixed-ADC based PMCW MIMO radar.

Index Terms—Cramér-Rao Bound (CRB), mixed-ADC based architecture, maximum likelihood (ML) estimation, mLIKES, one-bit ADC, PMCW MIMO radar.

I. INTRODUCTION

Millimeter-wave radar is an indispensable sensor for automotive radar applications, including advanced driver assistance and autonomous driving. Compared with other sensors, such as camera and lidar, radar can provide excellent sensing capabilities even in poor lighting or adverse weather conditions [1].

Multiple-input multiple-output (MIMO) radar can achieve high angular resolution with a relatively small number of antennas [2–4], and MIMO radar has become a standard for automotive radar applications. Because of the low-cost

advantage, most of the existing automotive radar are linear frequency-modulated continuous-wave (LFMCW) MIMO radar systems. However, with the increasing popularity of automotive radar, the mutual interference problems become increasingly severe [5]. Due to the code-division multiple access (CDMA) type of interference mitigation advantages, phase-modulated continuous-wave (PMCW) MIMO radar systems are attracting increasing attention in the literature [1, 5]. However, compared with LFMCW systems, PMCW systems require the receiver analog-to-digital converters (ADC's) to have a much higher sampling rate [1].

PMCW MIMO radar systems are typically required to sample the received signal at twice the bandwidth of the transmitted signal. Automotive radar systems typically operate in the millimeter-wave frequency range between 77–81 GHz, with a maximum bandwidth of 4 GHz [5]. At higher carrier frequencies, such as at 140 GHz under development by IMEC [6], the radar bandwidth can be much larger than the current maximum of 4 GHz. However, high rate and high precision ADC's are both expensive and power hungry [7, 8]. High level autonomous driving requires high angular resolution, making it necessary to deploy a large number of receive antennas, and hence a large number of ADC's, further increasing the cost and power consumption of the PMCW MIMO automotive radar.

Using low quantization resolution ADC's (e.g., 1–4 bits) at the receiver [9–13] is a promising approach to mitigate the aforementioned ADC problems because of their low cost and low power consumption advantages. However, low-precision ADC's suffer from dynamic range problems, i.e., a strong target can mask a weak target due to the high quantization errors [7, 14]. Yet high dynamic range is required for high-performance automotive radar applications. To mitigate the dynamic range problems of low-bit ADC's, we consider herein a mixed-ADC based architecture, in which most receive antenna outputs are sampled by one-bit ADC's, and one or a few outputs by high-resolution ADC's, for PMCW MIMO radar systems. The main contributions of this paper can be summarized as follows:

We first derive the Cramér-Rao bound (CRB) for the mixed-ADC based architecture for PMCW MIMO radar to characterize its best achievable performance for an unbiased target parameter estimator. Moreover, upper and lower bounds are provided on the CRB of the mixed-ADC system. The CRB analysis demonstrates that the mixed-ADC based architecture with a relatively small number of high-precision ADC's and a large number of one-bit ADC's can overcome the dynamic range problems of one-bit or low-bit sampling.

We next introduce a two-step estimator to realize the com-

This work was supported in part by the Youth Innovation Promotion Association CAS (CX2100060053), in part by the Anhui Provincial Natural Science Foundation under Grant 2208085J17, and in part by the National Natural Science Foundation of China under Grant 62271461.

X. Shang, R. Lin and Y. Cheng are with the Department of Electronic Engineering and Information Science, University of Science and Technology of China, Hefei 230027, China (e-mail: xlshang@mail.ustc.edu.cn, lrh23703@mail.ustc.edu.cn and cyb967@mail.ustc.edu.cn).

putationally efficient maximum likelihood (ML) estimation of the target parameters. Firstly, we formulate the angle-Doppler estimation problem encountered in the mixed-ADC based system as a sparse parameter estimation problem, and introduce a likelihood-based estimation approach, referred to as the mLIKES algorithm, for accurate angle-Doppler imaging. We use the majorization-minimization (MM) technique [15–19], which can transform a difficult optimization problem into a sequence of much simpler ones, to simply the optimization problem encountered in mLIKES to attain enhanced computational efficiency. By making use of the majorization-minimization technique [16, 19], the parameters can be updated iteratively. Moreover, the Nesterov acceleration technique [20, 21] is adopted to accelerate the convergence rate of the MM iterations. Furthermore, a RELAX-based approach is devised to further refine the results of mLIKES. Finally, we use numerical examples to demonstrate that mLIKES and RELAX-based refinement can be combined to obtain accurate target parameter estimates, with accuracy approaching the corresponding CRB.

The rest of this paper is organized as follows. A mixed-ADC based PMCW MIMO radar system is introduced in Section II. The CRB for the target parameters is derived in Section III. We introduce a two-step estimator to accurate target angle-Doppler parameter estimation in Section IV. The numerical examples are presented in Section V and Section VI concludes this paper.

Notation: We denote vectors and matrices by bold lowercase and uppercase letters, respectively. $(\cdot)^*$, $(\cdot)^T$ and $(\cdot)^H$ represent the complex conjugate, transpose and the conjugate transpose, respectively. $\mathbf{R} \in \mathbb{R}^{N \times M}$ or $\mathbf{R} \in \mathbb{C}^{N \times M}$ denotes a real or complex-valued $N \times M$ matrix. $\mathbf{A} \otimes \mathbf{B}$, $\mathbf{A} \odot \mathbf{B}$ and $\mathbf{A} \oplus \mathbf{B}$ denote, respectively, the Kronecker, Hadamard and Khatri–Rao matrix products. $\mathbf{A}[\delta, :]$ and $\mathbf{a}(\delta)$, respectively, extract rows and elements corresponding to the non-zero values of the logical array δ . $\text{vec}(\cdot)$ refers to the column-wise vectorization operation and $\text{diag}(\mathbf{d})$ denotes a diagonal matrix with diagonal entries formed from \mathbf{d} . $\text{tr}\{\mathbf{R}\}$ and $|\mathbf{R}|$, respectively, denote the trace and determinant of a square matrix \mathbf{R} . $\mathbf{A} \succeq \mathbf{B}$ means that $\mathbf{A} - \mathbf{B}$ is a positive semidefinite matrix. Denote $\mathbf{1}_N = [1, \dots, 1]^T \in \mathbb{R}^{N \times 1}$. \mathbf{I}_N denotes the $N \times N$ identity matrix and \mathbf{e}_n is the n -th column of \mathbf{I}_N . $A_R = \Re\{A\}$ and $A_I = \Im\{A\}$, where $\Re\{\cdot\}$ and $\Im\{\cdot\}$ denote taking the real and imaginary parts, respectively. Finally, $j \triangleq \sqrt{-1}$.

II. PROBLEM FORMULATION

Consider a PMCW MIMO radar system with M_t transmit antennas and M_r receive antennas. As shown in Fig. 1, the PMCW MIMO radar uses M_t antennas to simultaneously transmit the same fast-time binary sequence after multiplying it with a unimodular random slow-time code that is unique for each transmit antenna and changes from one pulse repetition interval (PRI) to another within the coherent processing interval (CPI)¹. Let $\mathbf{a}_t(\theta)$ and $\mathbf{a}_r(\theta)$, respectively, denote the

¹Herein waveform orthogonality is achieved by using slow-time code division multiplexing, which uses low-rate pseudorandom codes, changing from one PRI to another. This approach is low-cost and may be preferred in diverse applications.

transmit and receive steering vectors for a target at an azimuth angle θ :

$$\mathbf{a}_t(\theta) = [1, e^{-j2\pi \frac{d_t}{\lambda} \sin \theta}, \dots, e^{-j2\pi \frac{d_t}{\lambda} (M_t-1) \sin \theta}]^T \in \mathbb{C}^{M_t \times 1} \quad (1)$$

and

$$\mathbf{a}_r(\theta) = [1, e^{-j2\pi \frac{d_r}{\lambda} \sin \theta}, \dots, e^{-j2\pi \frac{d_r}{\lambda} (M_r-1) \sin \theta}]^T \in \mathbb{C}^{M_r \times 1} \quad (2)$$

where λ is the wavelength; d_t and d_r represent the inter-element distances of the transmit and receive uniform linear arrays, respectively. Assume that a total number of N PRI's are used during a CPI to determine the Doppler shifts of moving targets. A nominal slow-time temporal steering vector $\mathbf{d}(\omega)$ for a target with Doppler frequency shift ω can be written as:

$$\mathbf{d}(\omega) = [1, e^{j\omega}, \dots, e^{j(N-1)\omega}]^T \in \mathbb{C}^{N \times 1}. \quad (3)$$

At a given fixed fast-time, the data received by such a PMCW

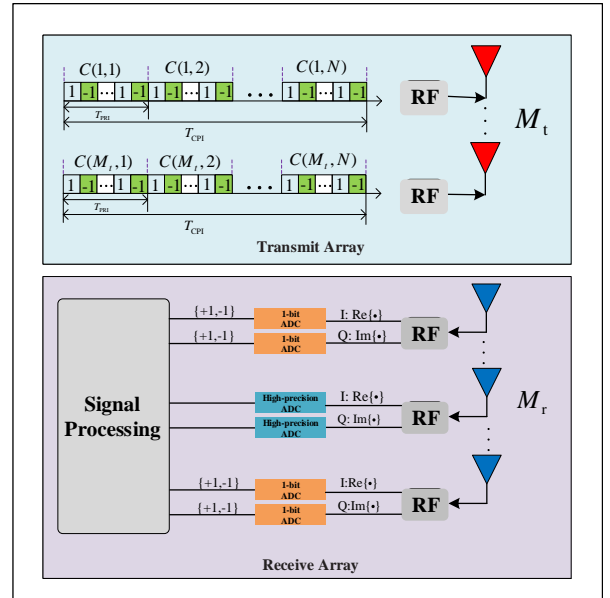


Fig. 1. The mixed-ADC based PMCW MIMO radar architecture.

MIMO radar in the slow-time and angular domain can be written as:

$$\mathbf{X} = \sum_{k=1}^K \mathbf{a}_r(\theta_k) b_k (\mathbf{C}^T \mathbf{a}_t(\theta_k) \odot \mathbf{d}(\omega_k))^T + \mathbf{E} \in \mathbb{C}^{M_r \times N}, \quad (4)$$

where $\{\theta_k\}_{k=1}^K$ and $\{\omega_k\}_{k=1}^K$ represent the azimuth angles and Doppler shifts of K targets, respectively; $\{b_k\}_{k=1}^K$ are the complex-valued amplitudes, which are proportional to the radar-cross-sections (RCS) of the targets; $\mathbf{C} \in \mathbb{C}^{M_t \times N}$ represents the slow-time code matrix, with the (m, n) th element, $C(m, n) = e^{j\phi_{m,n}}$, denoting the slow-time code for the m th antenna at the n th PRI; and \mathbf{E} is the unknown additive noise matrix. The extension to the case of joint range-Doppler-angle estimation is not difficult but it leads to more complicated expressions. To keep the exposition herein as simple as possible, we will only consider angle-Doppler imaging herein.

The observed data matrix can also be expressed compactly as follows:

$$\begin{aligned}\mathbf{X} &= \mathbf{A}_r \mathbf{B} (\mathbf{C}^T \mathbf{A}_t \odot \mathbf{D})^T + \mathbf{E} \\ &= \mathbf{A}_r \mathbf{B} \mathbf{V}^T + \mathbf{E},\end{aligned}\quad (5)$$

where

$$\begin{aligned}\mathbf{A}_r &= [\mathbf{a}_r(\theta_1), \dots, \mathbf{a}_r(\theta_K)] \in \mathbb{C}^{M_r \times K}, \\ \mathbf{A}_t &= [\mathbf{a}_t(\theta_1), \dots, \mathbf{a}_t(\theta_K)] \in \mathbb{C}^{M_t \times K}, \\ \mathbf{D} &= [\mathbf{d}(\omega_1), \dots, \mathbf{d}(\omega_K)] \in \mathbb{C}^{N \times K}, \\ \mathbf{V} &\triangleq \mathbf{C}^T \mathbf{A}_t \odot \mathbf{D} \in \mathbb{C}^{N \times K},\end{aligned}\quad (6)$$

and

$$\begin{aligned}\mathbf{b} &= [b_1, \dots, b_K]^T, \\ \mathbf{B} &= \text{diag}(\mathbf{b}).\end{aligned}\quad (7)$$

Let the vectors $\boldsymbol{\theta}$ and $\boldsymbol{\omega}$ collect the target azimuth angles and Doppler frequencies, respectively. When there is no risk for confusion, we omit the dependence of different functions (such as $\mathbf{A}_r(\boldsymbol{\theta})$ on $\boldsymbol{\theta}$) to simplify the notation. Let $\mathbf{x} = \text{vec}(\mathbf{X})$ and $\mathbf{e} = \text{vec}(\mathbf{E})$. The data model in (5) is equivalent to:

$$\begin{aligned}\mathbf{x} &= \sum_{k=1}^K b_k \mathbf{v}(\theta_k, \omega_k) \otimes \mathbf{a}_r(\theta_k) + \mathbf{e} \\ &= \sum_{k=1}^K b_k \left[(\mathbf{C}^T \mathbf{a}_t(\theta_k)) \odot \mathbf{d}(\omega_k) \right] \otimes [\mathbf{a}_r(\theta_k) \odot \mathbf{1}_{M_r}] + \mathbf{e} \\ &= \sum_{k=1}^K b_k \left[(\mathbf{C}^T \mathbf{a}_t(\theta_k)) \otimes \mathbf{a}_r(\theta_k) \right] \odot [\mathbf{d}(\omega_k) \otimes \mathbf{1}_{M_r}] + \mathbf{e} \\ &= \sum_{k=1}^K b_k \left[(\mathbf{C}^T \otimes \mathbf{I}_{M_r}) (\mathbf{a}_t(\theta_k) \otimes \mathbf{a}_r(\theta_k)) \right] \odot [\mathbf{d}(\omega_k) \otimes \mathbf{1}_{M_r}] + \mathbf{e},\end{aligned}\quad (8)$$

where $\mathbf{v}(\theta_k, \omega_k)$ is the k th column of \mathbf{V} ; and the third and fourth equalities above, respectively, are obtained by using the following mixed-product properties:

$$(\mathbf{A} \odot \mathbf{C}) \otimes (\mathbf{B} \odot \mathbf{D}) = (\mathbf{A} \otimes \mathbf{B}) \odot (\mathbf{C} \otimes \mathbf{D}), \quad (9)$$

and

$$(\mathbf{A} \mathbf{C}) \otimes (\mathbf{B} \mathbf{D}) = (\mathbf{A} \otimes \mathbf{B}) (\mathbf{C} \otimes \mathbf{D}). \quad (10)$$

Note from (8) that the virtual aperture $\mathbf{a}_t(\theta_k) \otimes \mathbf{a}_r(\theta_k)$ is linearly mapped to $(\mathbf{C}^T \otimes \mathbf{I}_{M_r}) (\mathbf{a}_t(\theta_k) \otimes \mathbf{a}_r(\theta_k))$ by the matrix $\mathbf{C}^T \otimes \mathbf{I}_{M_r}$, but the angle and Doppler information are coupled via the Hadamard product.

A. One-bit Quantization

When all antennas adopt one-bit quantization at the receivers, we obtain the signed measurement matrix $\mathbf{Z} = \mathbf{Z}_R + j\mathbf{Z}_I$ by comparing the unquantized received signal \mathbf{X} with a known time-varying threshold $\mathbf{H} \in \mathbb{C}^{M_r \times N}$ [12]:

$$\mathbf{Z} = \text{signc}(\mathbf{X} - \mathbf{H}), \quad (11)$$

where $\text{signc}(x) = \text{sign}(\text{Re}[x]) + j\text{sign}(\text{Im}[x])$ and $\text{sign}(x)$ is the element-wise sign operator defined as:

$$\text{sign}(x) = \begin{cases} 1 & x \geq 0, \\ -1 & x < 0. \end{cases} \quad (12)$$

B. Mixed-ADC Quantization

As shown in Fig. 1, we also consider a mixed-ADC based architecture in which only L pairs of ADC's are high-precision and all other $(M_r - L)$ pairs are one-bit ADC's. For the convenience of subsequent processing, we define a high-precision ADC indicator vector $\boldsymbol{\delta} = [\delta_1, \dots, \delta_{M_r}]^T$ with $\delta_m \in \{0, 1\}$, where $\delta_m = 1$ means that the m -th antenna output is sampled by a pair of high-precision ADC's (for its I (in-phase) and Q (quadrature) channels), whereas $\delta_m = 0$ indicates one-bit ADC's. Then, the mixed-ADC quantized output is:

$$\mathbf{Y} = \text{diag}(\boldsymbol{\delta})\mathbf{X} + \text{diag}(\bar{\boldsymbol{\delta}})\mathbf{Z}, \quad (13)$$

where $\bar{\boldsymbol{\delta}} = \mathbf{1}_{M_r} - \boldsymbol{\delta}$ is a one-bit ADC indicator. For later use, we separate mixed-ADC outputs into the high-precision group $\mathbf{Y}_0 = \mathbf{Y}[\boldsymbol{\delta}, :] \in \mathbb{C}^{L \times N}$ and the one-bit group $\mathbf{Y}_1 = \mathbf{Y}[\bar{\boldsymbol{\delta}}, :] \in \mathbb{C}^{(M_r-L) \times N}$. Let $\mathbf{y}_0 = \text{vec}(\mathbf{Y}_0)$ and $\mathbf{y}_1 = \text{vec}(\mathbf{Y}_1)$. Then \mathbf{y}_0 and \mathbf{y}_1 , respectively, have the following expressions:

$$\mathbf{y}_0 = \sum_{k=1}^K b_k \mathbf{a}_0(\theta_k, \omega_k) + \mathbf{e}_0 \in \mathbb{C}^{NL \times 1},$$

and

$$\mathbf{y}_1 = \text{signc}\left(\sum_{k=1}^K b_k \mathbf{a}_1(\theta_k, \omega_k) - \mathbf{h}_1 + \mathbf{e}_1\right) \in \mathbb{C}^{N(M_r-L) \times 1}, \quad (14)$$

where $\mathbf{a}_0(\theta_k, \omega_k) \triangleq \mathbf{v}(\theta_k, \omega_k) \otimes \tilde{\mathbf{a}}_r(\theta_k)$; $\mathbf{a}_1(\theta_k, \omega_k) \triangleq \mathbf{v}(\theta_k, \omega_k) \otimes \tilde{\mathbf{a}}_r(\theta_k)$; $\tilde{\mathbf{a}}_r(\theta_k)$ and $\tilde{\mathbf{a}}_r(\theta_k)$ are sub-vectors extracted from $\mathbf{a}_r(\theta_k)$ via the vectors $\boldsymbol{\delta}$ and $\bar{\boldsymbol{\delta}}$, respectively; \mathbf{e}_0 and \mathbf{e}_1 represent the additive noise; and $\mathbf{h}_1 \triangleq \text{vec}(\mathbf{H}[\bar{\boldsymbol{\delta}}, :])$ is the time-varying threshold vector adopted by one-bit ADC's.

Our problem of interest herein is to estimate the unknown target parameters and form angle-Doppler images from the mixed-ADC output matrix \mathbf{Y} .

III. CRAMÉR-RAO BOUND

Let $\boldsymbol{\varphi}$ collect all the real-valued unknown target parameters, i.e., $\boldsymbol{\varphi} = [\boldsymbol{\theta}^T, \boldsymbol{\omega}^T, \mathbf{b}_R^T, \mathbf{b}_I^T]^T \in \mathbb{R}^{4K \times 1}$. When the noise power σ^2 is unknown, the unknown parameter vector becomes $\boldsymbol{\zeta} = [\boldsymbol{\varphi}^T, \sigma]^T \in \mathbb{R}^{(4K+1) \times 1}$. Under the assumption that \mathbf{E} is the circularly symmetric complex-valued white Gaussian noise with i.i.d. $\mathcal{CN}(0, \sigma^2)$ entries, the log-likelihood function of the measurement matrix \mathbf{Y} is given by:

$$\ln L(\boldsymbol{\zeta}) = \ln L_0(\boldsymbol{\zeta}) + \ln L_1(\boldsymbol{\zeta}), \quad (15)$$

where $L_0(\boldsymbol{\zeta})$ and $L_1(\boldsymbol{\zeta})$ represent the likelihood functions of the high-precision and one-bit measurements, respectively. The Fisher information matrix (FIM) for the mixed-ADC system can be written as:

$$\mathbf{F}_m = \mathbb{E} \left[\frac{\partial \ln L(\boldsymbol{\zeta})}{\partial \boldsymbol{\zeta}} \frac{\partial \ln L(\boldsymbol{\zeta})}{\partial \boldsymbol{\zeta}^T} \right]. \quad (16)$$

It follows from (15) that

$$\begin{aligned} \mathbf{F}_m = & \mathbb{E} \left[\frac{\partial \ln L_0(\zeta)}{\partial \zeta} \frac{\partial \ln L_0(\zeta)}{\partial \zeta^T} \right] + \mathbb{E} \left[\frac{\partial \ln L_1(\zeta)}{\partial \zeta} \frac{\partial \ln L_1(\zeta)}{\partial \zeta^T} \right] \\ & + \mathbb{E} \left[\frac{\partial \ln L_0(\zeta)}{\partial \zeta} \frac{\partial \ln L_1(\zeta)}{\partial \zeta^T} \right] + \mathbb{E} \left[\frac{\partial \ln L_1(\zeta)}{\partial \zeta} \frac{\partial \ln L_0(\zeta)}{\partial \zeta^T} \right]. \end{aligned} \quad (17)$$

Using the fact that the noise entries $\{E(m, n)\}$ are independent random variables, we obtain:

$$\begin{aligned} \mathbb{E} \left[\frac{\partial \ln L_0(\zeta)}{\partial \zeta} \frac{\partial \ln L_1(\zeta)}{\partial \zeta^T} \right] &= \underbrace{\mathbb{E} \left[\frac{\partial \ln L_0(\zeta)}{\partial \zeta} \right]}_{=0} \underbrace{\mathbb{E} \left[\frac{\partial \ln L_1(\zeta)}{\partial \zeta^T} \right]}_{=0} \\ &= \mathbf{0}. \end{aligned} \quad (18)$$

Inserting (18) into (17) yields the following expression for \mathbf{F}_m :

$$\mathbf{F}_m = \mathbb{E} \left[\frac{\partial \ln L_0(\zeta)}{\partial \zeta} \frac{\partial \ln L_0(\zeta)}{\partial \zeta^T} \right] + \mathbb{E} \left[\frac{\partial \ln L_1(\zeta)}{\partial \zeta} \frac{\partial \ln L_1(\zeta)}{\partial \zeta^T} \right]. \quad (19)$$

Equation (19) demonstrates the fact that the FIM for the mixed-ADC outputs is the summation of the FIMs for the high-precision outputs and one-bit outputs. In the next two subsections, we focus on the derivations of the FIMs for high-precision outputs and one-bit outputs. Then, the FIM for the mixed-ADC outputs can be readily obtained.

A. Cramér-Rao Bound for High-precision Data

1) *Known noise variance:* The FIM for the high-precision outputs with respect to φ in (4) can be written as (see Appendix A for the detailed derivations):

$$\mathbf{F}_0(\varphi) = \frac{2}{\sigma^2} \Re \left\{ \begin{bmatrix} \mathbf{F}_{11} & \mathbf{F}_{12} & \mathbf{F}_{13} & j\mathbf{F}_{13} \\ \mathbf{F}_{12}^T & \mathbf{F}_{22} & \mathbf{F}_{23} & j\mathbf{F}_{23} \\ \mathbf{F}_{13}^T & \mathbf{F}_{23}^T & \mathbf{F}_{33} & j\mathbf{F}_{33} \\ j\mathbf{F}_{13}^T & j\mathbf{F}_{23}^T & j\mathbf{F}_{33}^T & \mathbf{F}_{33} \end{bmatrix} \right\}, \quad (20)$$

where

$$\begin{aligned} \mathbf{F}_{11} = & (\dot{\mathbf{A}}_r^H \dot{\mathbf{A}}_r) \odot (\mathbf{B}^* \mathbf{V}^H \mathbf{V} \mathbf{B}) + (\dot{\mathbf{A}}_r^H \mathbf{A}_r) \odot (\mathbf{B}^* \mathbf{V}^H \dot{\mathbf{V}}_\theta \mathbf{B}) \\ & + (\mathbf{A}_r^H \dot{\mathbf{A}}_r) \odot (\mathbf{B}^* \dot{\mathbf{V}}_\theta^H \mathbf{V} \mathbf{B}) + (\mathbf{A}_r^H \mathbf{A}_r) \odot (\mathbf{B}^* \dot{\mathbf{V}}_\theta^H \dot{\mathbf{V}}_\theta \mathbf{B}), \end{aligned} \quad (21)$$

$$\mathbf{F}_{12} = (\dot{\mathbf{A}}_r^H \mathbf{A}_r) \odot (\mathbf{B}^* \mathbf{V}^H \dot{\mathbf{V}}_\omega \mathbf{B}) + (\mathbf{A}_r^H \dot{\mathbf{A}}_r) \odot (\mathbf{B}^* \dot{\mathbf{V}}_\theta^H \dot{\mathbf{V}}_\omega \mathbf{B}), \quad (22)$$

$$\mathbf{F}_{13} = (\dot{\mathbf{A}}_r^H \mathbf{A}_r) \odot (\mathbf{B}^* \mathbf{V}^H \mathbf{V}) + (\mathbf{A}_r^H \dot{\mathbf{A}}_r) \odot (\mathbf{B}^H \dot{\mathbf{V}}_\theta \mathbf{V}), \quad (23)$$

$$\mathbf{F}_{22} = (\mathbf{A}_r^H \mathbf{A}_r) \odot (\mathbf{B}^* \dot{\mathbf{V}}_\omega^H \dot{\mathbf{V}}_\omega \mathbf{B}), \quad (24)$$

$$\mathbf{F}_{23} = (\mathbf{A}_r^H \mathbf{A}_r) \odot (\mathbf{B}^* \dot{\mathbf{V}}_\omega^H \mathbf{V}), \quad (25)$$

$$\mathbf{F}_{33} = (\mathbf{A}_r^H \mathbf{A}_r) \odot (\mathbf{V}^H \mathbf{V}), \quad (26)$$

and

$$\dot{\mathbf{A}}_r = \left[\frac{\partial \mathbf{a}_r(\theta_1)}{\partial \theta_1}, \dots, \frac{\partial \mathbf{a}_r(\theta_K)}{\partial \theta_K} \right], \quad (27)$$

$$\dot{\mathbf{V}}_\theta = \left[\frac{\partial \mathbf{v}(\theta_1, \omega_1)}{\partial \theta_1}, \dots, \frac{\partial \mathbf{v}(\theta_K, \omega_K)}{\partial \theta_K} \right], \quad (28)$$

$$\dot{\mathbf{V}}_\omega = \left[\frac{\partial \mathbf{v}(\theta_1, \omega_1)}{\partial \omega_1}, \dots, \frac{\partial \mathbf{v}(\theta_K, \omega_K)}{\partial \omega_K} \right]. \quad (29)$$

2) *Unknown noise variance:* When the noise power σ^2 is unknown, the FIM for estimating ζ is given by:

$$\mathbf{F}_0(\zeta) = \begin{bmatrix} \mathbf{F}_0(\varphi) & \mathbf{0} \\ \mathbf{0} & \frac{4NM_r}{\sigma^2} \end{bmatrix},$$

which is a block diagonal matrix. Hence, the CRB matrix for the high precision data of both the known and unknown noise power cases is given by:

$$\mathbf{CRB}_0(\varphi) = \mathbf{F}_0^{-1}(\varphi). \quad (30)$$

B. Cramér-Rao Bound for One-Bit Data

1) *Known noise variance:* Making use of the property of Hadamard product: $(\mathbf{A}\mathbf{C}) \odot (\mathbf{B}\mathbf{D}) = (\mathbf{A}^T \oplus \mathbf{B}^T)^T (\mathbf{C} \oplus \mathbf{D})$, the FIM $\mathbf{F}_0(\varphi)$ for the high-precision data in (20) can be rewritten as:

$$\mathbf{F}_0(\varphi) = \frac{2}{\sigma^2} \Re \{ \mathbf{U} \mathbf{U}^H \}, \quad (31)$$

where

$$\mathbf{U} = [\dot{\mathbf{A}}_r \oplus (\mathbf{V}\mathbf{B}) + \mathbf{A}_r \oplus (\dot{\mathbf{V}}_\theta \mathbf{B}), \mathbf{A}_r \oplus (\dot{\mathbf{V}}_\omega \mathbf{B}), \mathbf{A}_r \oplus \mathbf{V}, j\mathbf{A}_r \oplus \mathbf{V}]^H \in \mathbb{C}^{4K \times NM_r}. \quad (32)$$

The results presented in [14, 22] have indicated the connection between the FIM for one-bit quantizer $\mathbf{F}_1(\varphi)$ and that of the high-precision quantizer $\mathbf{F}_0(\varphi)$, from which and (31) we obtain the following expression for $\mathbf{F}_1(\varphi)$:

$$\mathbf{F}_1(\varphi) = \frac{1}{\pi \sigma^2} (\mathbf{U}_R \mathbf{\Lambda}_R \mathbf{U}_R^T + \mathbf{U}_I \mathbf{\Lambda}_I \mathbf{U}_I^T), \quad (33)$$

where $\mathbf{\Lambda} = \text{diag}([\lambda_1, \dots, \lambda_{NM_r}])$. Let $\mathbf{h} = \text{vec}(\mathbf{H})$ and $\boldsymbol{\mu} = \frac{\sum_{k=1}^K b_k \mathbf{v}(\theta_k, \omega_k) \otimes \mathbf{a}_r(\theta_k) - \mathbf{h}}{\sigma/\sqrt{2}} \in \mathbb{C}^{NM_r \times 1}$. Then, λ_k is given by:

$$\lambda_k = G(\mu_{R,k}) + jG(\mu_{I,k}), \quad (34)$$

where the function $G(x)$ is defined as:

$$G(x) = \left[\frac{1}{\Phi(x)} + \frac{1}{\Phi(-x)} \right] e^{-x^2}, \quad (35)$$

with $\Phi(x) = \int_{-\infty}^x \frac{1}{\sqrt{2\pi}} e^{-\frac{t^2}{2}} dt$ being the cumulative distribution function (cdf) of the normal standard distribution. The corresponding CRB for the one-bit measurements for the known σ^2 case is given by:

$$\mathbf{CRB}_1(\varphi) = \mathbf{F}_1^{-1}(\varphi). \quad (36)$$

We have proved in [14] that $0 < G(x) \leq 4$ and therefore $\mathbf{F}_1(\varphi) \preceq \frac{2}{\pi} \mathbf{F}_0(\varphi)$. Moreover, combining the upper bounds for one-bit FIM in [14], we have

$$\frac{2}{\pi} \mathbf{F}_{1,1}(\varphi) \preceq \mathbf{F}_1(\varphi) \preceq \frac{2}{\pi} \mathbf{F}_0(\varphi), \quad (37)$$

where $\mathbf{F}_{1,1}(\varphi) = \frac{2}{\sigma^2} (\mathbf{U}_R \bar{\mathbf{\Lambda}}_R \mathbf{U}_R^T + \mathbf{U}_I \bar{\mathbf{\Lambda}}_I \mathbf{U}_I^T)$ with $\bar{\mathbf{\Lambda}}$ being a diagonal matrix with its k -th diagonal element $\bar{\lambda}_k$ being:

$$\bar{\lambda}_k = e^{-\mu_{R,k}^2} + j e^{-\mu_{I,k}^2}. \quad (38)$$

Thus the one-bit CRB has the following lower and upper bounds:

$$\frac{\pi}{2} \mathbf{F}_{1,1}^{-1}(\varphi) \succeq \mathbf{CRB}_1(\varphi) \succeq \frac{\pi}{2} \mathbf{CRB}_0(\varphi). \quad (39)$$

2) *Unknown noise variance:* When the noise power σ^2 is unknown, the matrix \mathbf{U} can be expanded as $\bar{\mathbf{U}}$ with the following expression:

$$\bar{\mathbf{U}} = [\mathbf{U}^T \quad -(\mathbf{x} - \mathbf{h})/\sigma]^T \in \mathbb{C}^{(4K+1) \times NM_r}. \quad (40)$$

Then the FIM for estimating ζ is:

$$\begin{aligned} \mathbf{F}_1(\zeta) &= \begin{bmatrix} \mathbf{F}_1(\varphi) & \mathbf{F}_1(\varphi, \sigma) \\ \mathbf{F}_1^T(\varphi, \sigma) & F_1(\sigma, \sigma) \end{bmatrix} \\ &= \frac{1}{\pi\sigma^2} (\bar{\mathbf{U}}_R \mathbf{\Lambda}_R \bar{\mathbf{U}}_R^T + \bar{\mathbf{U}}_I \mathbf{\Lambda}_I \bar{\mathbf{U}}_I^T), \end{aligned} \quad (41)$$

and the $\mathbf{CRB}_1(\varphi)$ for the unknown σ^2 case is given by:

$$\mathbf{CRB}_1(\varphi) = [\mathbf{F}_1(\varphi) - \mathbf{F}_1(\varphi, \sigma) F_1^{-1}(\sigma, \sigma) \mathbf{F}_1^T(\varphi, \sigma)]^{-1}. \quad (42)$$

It can be easily verified that the inequality $\mathbf{CRB}_1(\varphi) \succeq \frac{\pi}{2} \mathbf{CRB}_0(\varphi)$ still holds for the unknown noise variance case.

C. Cramér-Rao Bound for Mixed-ADC based Output

1) *Known noise variance:* We can observe from (32) that the k th column of \mathbf{U} represents the contribution of the k th measurement x_k on the FIM of the high-precision outputs. Using the following definitions:

$$\begin{aligned} \mathbf{U}_0 &= \mathbf{U} \text{diag}(\boldsymbol{\delta} \otimes \mathbf{1}_N), \\ \mathbf{U}_1 &= \mathbf{U} \text{diag}(\bar{\boldsymbol{\delta}} \otimes \mathbf{1}_N), \end{aligned} \quad (43)$$

we obtain the following expression for the mixed-ADC based FIM:

$$\begin{aligned} \mathbf{F}_m(\varphi) &= \frac{2}{\sigma^2} \Re \{ \mathbf{U}_0 \mathbf{U}_0^H \} \\ &+ \frac{1}{\pi\sigma^2} (\mathbf{U}_{1,R} \mathbf{\Lambda}_R \mathbf{U}_{1,R}^T + \mathbf{U}_{1,I} \mathbf{\Lambda}_I \mathbf{U}_{1,I}^T), \end{aligned} \quad (44)$$

where the first and second terms of \mathbf{F}_m , respectively, represent the contributions of the high-precision and one-bit measurements to the mixed-ADC based FIM. The difference between the FIM for the mixed-ADC based outputs (i.e., $\mathbf{F}_m(\varphi)$) and that of the high precision outputs (i.e., $\mathbf{F}_0(\varphi)$) can be expressed as:

$$(\mathbf{F}_0 - \mathbf{F}_m)^{-1} = \mathbf{F}_0^{-1} - \mathbf{F}_0^{-1} (\mathbf{F}_0^{-1} - \mathbf{F}_m^{-1})^{-1} \mathbf{F}_0^{-1}, \quad (45)$$

where the dependence of \mathbf{F}_0 and \mathbf{F}_m on φ is omitted to simplify the notation; this dependence on φ will be reinstated when it becomes important. From (45), we have that

$$\mathbf{F}_0^{-1} - \mathbf{F}_m^{-1} = [\mathbf{F}_0 - \mathbf{F}_0 (\mathbf{F}_0 - \mathbf{F}_m)^{-1} \mathbf{F}_0]^{-1}. \quad (46)$$

Note that

$$\begin{aligned} \mathbf{F}_0 - \mathbf{F}_m &= \frac{2}{\sigma^2} \Re \{ \mathbf{U}_1 \mathbf{U}_1^H \} - \frac{1}{\pi\sigma^2} (\mathbf{U}_{1,R} \mathbf{\Lambda}_R \mathbf{U}_{1,R}^T + \mathbf{U}_{1,I} \mathbf{\Lambda}_I \mathbf{U}_{1,I}^T), \\ &\succeq \left(1 - \frac{2}{\pi}\right) \bar{\mathbf{F}}_0(\varphi), \end{aligned} \quad (47)$$

where $\bar{\mathbf{F}}_0(\varphi) \triangleq \frac{2}{\sigma^2} \Re \{ \mathbf{U}_1 \mathbf{U}_1^H \}$. Inserting (47) into (46), it is straightforward to obtain that

$$\mathbf{F}_m^{-1} \succeq \mathbf{F}_0^{-1} + \left[\frac{\pi}{\pi-2} \mathbf{F}_0 \bar{\mathbf{F}}_0^{-1} - \mathbf{I} \right]^{-1} \mathbf{F}_0^{-1}, \quad (48)$$

or, equivalently,

$$\mathbf{CRB}_m(\varphi) \succeq (\mathbf{I} + \mathbf{\Gamma}_1) \mathbf{CRB}_0(\varphi), \quad (49)$$

where $\mathbf{\Gamma}_1 \triangleq \left[\frac{\pi}{\pi-2} \mathbf{F}_0 \bar{\mathbf{F}}_0^{-1} - \mathbf{I} \right]^{-1}$. Combining the fact that $\mathbf{F}_0 \succ \bar{\mathbf{F}}_0$, $\mathbf{\Gamma}_1$ is a positive-definite matrix corresponding to the

loss paid for using one-bit ADC's. Moreover, $\bar{\mathbf{F}}_0^{-1}$ decreases as the number of one-bit ADC pairs (i.e. $M_r - L$) increase; hence $\mathbf{CRB}_m(\varphi)$ increases, indicating inferior parameter estimation performance, as the number of one-bit ADC pairs increases. Similarly, making use of the lower bound of the one-bit FIM in (37), we can get the following upper bound on $\mathbf{CRB}_m(\varphi)$:

$$\mathbf{CRB}_m(\varphi) \preceq (\mathbf{I} + \mathbf{\Gamma}_u) \mathbf{CRB}_0(\varphi), \quad (50)$$

where $\mathbf{\Gamma}_u \triangleq [\mathbf{F}_0 (\mathbf{F}_0 - \bar{\mathbf{F}}_{1,I})^{-1} - \mathbf{I}]^{-1}$ with

$$\bar{\mathbf{F}}_{1,I} = \mathbf{U}_{1,R} \bar{\mathbf{\Lambda}}_R \mathbf{U}_{1,R}^T + \mathbf{U}_{1,I} \bar{\mathbf{\Lambda}}_I \mathbf{U}_{1,I}^T, \quad (51)$$

and where $\bar{\mathbf{\Lambda}}$ is given in (38).

2) *Unknown noise variance:* When σ^2 is unknown, the FIM for estimating ζ is:

$$\begin{aligned} \mathbf{F}_m(\zeta) &= \begin{bmatrix} \mathbf{F}_m(\varphi) & \mathbf{F}_m(\varphi, \sigma) \\ \mathbf{F}_m^T(\varphi, \sigma) & F_m(\sigma, \sigma) \end{bmatrix} \\ &= \frac{2}{\sigma^2} \Re \left\{ \begin{bmatrix} \mathbf{U}_0 \mathbf{U}_0^H & \mathbf{0} \\ \mathbf{0} & 2NL \end{bmatrix} \right\} \\ &+ \frac{1}{\pi\sigma^2} (\bar{\mathbf{U}}_{1,R} \mathbf{\Lambda}_R \bar{\mathbf{U}}_{1,R}^T + \bar{\mathbf{U}}_{1,I} \mathbf{\Lambda}_I \bar{\mathbf{U}}_{1,I}^T), \end{aligned} \quad (52)$$

where $\bar{\mathbf{U}}_1 = \bar{\mathbf{U}} \text{diag}(\bar{\boldsymbol{\delta}} \otimes \mathbf{1}_N)$. Similar to the one-bit case, the CRB matrix for estimating φ using the mixed-ADC based measurements is given by:

$$\mathbf{CRB}_m(\varphi) = [\mathbf{F}_m(\varphi) - \mathbf{F}_m(\varphi, \sigma) F_m^{-1}(\sigma, \sigma) \mathbf{F}_m^T(\varphi, \sigma)]^{-1}. \quad (53)$$

Also, it can be readily checked that the lower bound shown in (49) still holds for this unknown noise variance case.

IV. MIXED-ADC BASED PARAMETER ESTIMATION

Consider first the maximum likelihood (ML) estimator, which is theoretically appealing due to its desirable properties including consistency and asymptotic efficiency. We assume that both $\mathbf{e}_0 \in \mathbb{C}^{NL \times 1}$ and $\mathbf{e}_1 \in \mathbb{C}^{N(M_r-L) \times 1}$ are circularly symmetric complex-valued white Gaussian noise with i.i.d. $\mathcal{CN}(0, \sigma^2)$ entries. The negative log-likelihood function for the model described in (14) is given by:

$$\begin{aligned} -\ln L(\zeta) &= -\ln L_0(\zeta) - \ln L_1(\zeta) \\ &= -\sum_{n=1}^{N(M_r-L)} \ln \left(\Phi \left(y_{1,R}(n) \frac{\Re\{\sum_{k=1}^K b_k a_{1,n}(\theta_k, \omega_k)\} - h_{1,R}(n)}{\sigma/\sqrt{2}} \right) \right) \\ &- \sum_{n=1}^{N(M_r-L)} \ln \left(\Phi \left(y_{1,I}(n) \frac{\Im\{\sum_{k=1}^K b_k a_{1,n}(\theta_k, \omega_k)\} - h_{1,I}(n)}{\sigma/\sqrt{2}} \right) \right) \\ &+ \frac{\|\mathbf{y}_0 - \sum_{k=1}^K b_k \mathbf{a}_0(\theta_k, \omega_k)\|^2}{\sigma^2} + NL \ln \sigma^2 + NL \ln \pi, \end{aligned} \quad (54)$$

where $a_{1,n}(\theta_k, \omega_k)$ represents the n -th element of the vector $\mathbf{a}_1(\theta_k, \omega_k)$. Let $\eta = 1/\sigma$ and $\boldsymbol{\beta} = \eta \mathbf{b}$. Then the negative log-likelihood function can be rewritten as:

$$\begin{aligned} -\ln L(\boldsymbol{\beta}, \boldsymbol{\omega}, \boldsymbol{\theta}, \eta) &= -\sum_{n=1}^{N(M_r-L)} \ln \left(\Phi \left(y_{1,R}(n) \sqrt{2} \left[\Re\left\{ \sum_{k=1}^K \beta_k a_{1,n}(\theta_k, \omega_k) \right\} - \eta h_{1,R}(n) \right] \right) \right) \\ &- \sum_{n=1}^{N(M_r-L)} \ln \left(\Phi \left(y_{1,I}(n) \sqrt{2} \left[\Im\left\{ \sum_{k=1}^K \beta_k a_{1,n}(\theta_k, \omega_k) \right\} - \eta h_{1,I}(n) \right] \right) \right) \\ &+ \|\eta \mathbf{y}_0 - \sum_{k=1}^K \beta_k \mathbf{a}_0(\theta_k, \omega_k)\|^2 - NL \ln \eta^2 + NL \ln \pi. \end{aligned} \quad (55)$$

The negative log-likelihood function has a complicated form and is highly nonlinear and nonconvex with regard to $\boldsymbol{\theta}$ and $\boldsymbol{\omega}$. Therefore, the global minimization of $-\ln L(\boldsymbol{\beta}, \boldsymbol{\omega}, \boldsymbol{\theta}, \eta)$ is a challenging problem. For given $\boldsymbol{\theta}$ and $\boldsymbol{\omega}$, however, the above optimization problem is convex with regard to $\boldsymbol{\beta}$ and η and hence can be globally and efficiently solved using, e.g., the Newton method. Consequently, the ML estimator can be directly implemented as follows:

- A. Perform a $2K$ -dimensional exhaustive coarse search on the angular and Doppler spaces to find coarse estimates of both $\boldsymbol{\theta}$ and $\boldsymbol{\omega}$.
- B. Determine the corresponding optimal estimates of $\boldsymbol{\beta}$ and η for given estimates of $\boldsymbol{\theta}$ and $\boldsymbol{\omega}$.
- C. Refine the results by using an efficient fine search method over narrow intervals near the coarse angle and Doppler estimates.

Regarding Step A, we consider a direct grid-based implementation. Assume that the angular and Doppler domains are, respectively, grided into K_θ and K_ω points. Then the optimization problem of estimating $\boldsymbol{\beta}$ and η for given estimates of $\boldsymbol{\theta}$ and $\boldsymbol{\omega}$ needs to be solved $(K_\theta K_\omega)^K$ times and the parameters with the minimum negative log-likelihood value are chosen as their estimates. As the number of targets increases, the complexity required by step A becomes computationally prohibitive. We present next an efficient strategy to realize the ML estimation.

A. mLIKES for Sparse Parameter Estimation

We uniformly discretize the continuous angular and Doppler space into K_θ and K_ω grid points, respectively. To attain high resolution, the typical choices of K_θ and K_ω are $4M_r \leq K_\theta \leq 10M_r$ and $4N \leq K_\omega \leq 10N$, respectively. The number of targets, i.e., K , is usually much smaller than $K_\theta K_\omega$. Therefore we can formulate the data model in (8), at least approximately, as the following sparse linear model:

$$\mathbf{x} = \mathbf{A}\boldsymbol{\alpha} + \mathbf{e} \in \mathbb{C}^{NM_r}, \quad \mathbf{A} \in \mathbb{C}^{NM_r \times K_\theta K_\omega}, \quad (56)$$

where $\mathbf{A} = [\mathbf{a}(\tilde{\theta}_1, \tilde{\omega}_1), \dots, \mathbf{a}(\tilde{\theta}_{K_\theta}, \tilde{\omega}_{K_\omega}), \dots, \mathbf{a}(\tilde{\theta}_{K_\theta}, \tilde{\omega}_{K_\omega})]$, with $\mathbf{a}(\tilde{\theta}_{k_\theta}, \tilde{\omega}_{k_\omega})$ defined as:

$$\mathbf{a}(\tilde{\theta}_{k_\theta}, \tilde{\omega}_{k_\omega}) = \left[(\mathbf{C}^T \otimes \mathbf{I}_{M_r}) (\mathbf{a}_t(\tilde{\theta}_{k_\theta}) \otimes \mathbf{a}_r(\tilde{\theta}_{k_\theta})) \right] \odot [\mathbf{d}(\tilde{\omega}_{k_\omega}) \otimes \mathbf{1}_{M_r}], \quad (57)$$

and $\boldsymbol{\alpha} \in \mathbb{C}^{K_\theta K_\omega}$ is an unknown sparse vector with many zero elements. The non-zero elements of $\boldsymbol{\alpha}$ correspond to the target parameters. It follows from (8) and (56) that (14) can also be rewritten as:

$$\begin{aligned} \mathbf{y}_0 &= \mathbf{A}_0 \boldsymbol{\alpha} + \mathbf{e}_0 \in \mathbb{C}^{NL \times 1}, \\ \mathbf{y}_1 &= \text{signc}(\mathbf{A}_1 \boldsymbol{\alpha} - \mathbf{h}_1 + \mathbf{e}_1) \in \mathbb{C}^{N(M_r-L) \times 1}, \end{aligned} \quad (58)$$

where $\mathbf{A}_0 \triangleq \mathbf{A}[\boldsymbol{\delta} \otimes \mathbf{1}_N, :] \in \mathbb{C}^{NL \times K_\theta K_\omega}$ and $\mathbf{A}_1 = \mathbf{A}[\tilde{\boldsymbol{\delta}} \otimes \mathbf{1}_N, :] \in \mathbb{C}^{N(M_r-L) \times K_\theta K_\omega}$, respectively, correspond to the dictionary matrices of the high-precision measurements and the one-bit measurements. To enhance the robustness of mLIKES, we allow the noise of the high-precision outputs and that of the one-bit outputs to have different powers (namely $\mathbf{e}_0 \sim \mathcal{CN}(\mathbf{0}, \sigma_0^2 \mathbf{I}_{NL})$ and $\mathbf{e}_1 \sim \mathcal{CN}(\mathbf{0}, \sigma_1^2 \mathbf{I}_{N(M_r-L)})$). Let

$\eta_1 = 1/\sigma_1$. From (58), the negative log-likelihood function of the one-bit measurements is:

$$\begin{aligned} -\ln L_1(\boldsymbol{\alpha}, \eta_1) &= - \sum_{n=1}^{N(M_r-L)} \ln \Phi \left(y_{1,R}(n) \sqrt{2} \eta_1 \Re \left[\mathbf{a}_{1,n}^T \boldsymbol{\alpha} - h_1(n) \right] \right) \\ &\quad - \sum_{n=1}^{N(M_r-L)} \ln \Phi \left(y_{1,I}(n) \sqrt{2} \eta_1 \Im \left[\mathbf{a}_{1,n}^T \boldsymbol{\alpha} - h_1(n) \right] \right), \end{aligned} \quad (59)$$

where $\mathbf{a}_{1,n}$ is the n -th column of \mathbf{A}_1^T .

Then, taking into account the sparse property of the signal model, we minimize the following objective function for sparse parameter estimation:

$$\begin{aligned} \Psi(\boldsymbol{\alpha}, \eta_1, \sigma_0, \mathbf{p}) &= -\ln L_1(\boldsymbol{\alpha}, \eta_1) + \frac{1}{\sigma_0^2} \|\mathbf{A}_0 \boldsymbol{\alpha} - \mathbf{y}_0\|^2 \\ &\quad + \sum_{k=1}^{K_\theta K_\omega} \frac{|\alpha_k|^2}{p_k} + \ln |\mathbf{R}|, \end{aligned} \quad (60)$$

where

$$\begin{aligned} \mathbf{R} &= \begin{bmatrix} \mathbf{A}_0 \\ \mathbf{A}_1 \end{bmatrix} \mathbf{P} \begin{bmatrix} \mathbf{A}_0^H & \mathbf{A}_1^H \end{bmatrix} + \begin{bmatrix} \sigma_0^2 \mathbf{I}_{NL} & \mathbf{0} \\ \mathbf{0} & \frac{1}{\eta_1^2} \mathbf{I}_{N(M_r-L)} \end{bmatrix} \\ &= \tilde{\mathbf{A}} \mathbf{P} \tilde{\mathbf{A}}^H + \boldsymbol{\Sigma} \end{aligned} \quad (61)$$

and

$$\begin{aligned} \tilde{\mathbf{A}} &\triangleq [\mathbf{A}_0^T \quad \mathbf{A}_1^T]^T \\ \boldsymbol{\Sigma} &= \text{diag} \left(\left[\sigma_0^2 \mathbf{1}_{NL}^T, \quad 1/\eta_1^2 \mathbf{1}_{N(M_r-L)}^T \right]^T \right) \\ \mathbf{P} &= \text{diag}(\mathbf{p}), \quad \mathbf{p} = [p_1, \dots, p_{K_\theta K_\omega}]^T. \end{aligned} \quad (62)$$

The first term in (60), i.e., $-\ln L_1(\boldsymbol{\alpha}, \eta_1)$, is the fitting term of the one-bit measurements; the second term $\frac{1}{\sigma_0^2} \|\mathbf{A}_0 \boldsymbol{\alpha} - \mathbf{y}_0\|^2$ represents the least-squares fitting term of the high-precision measurements; and $\ln |\mathbf{R}|$ serves as the sparsity enforcing term. Note that the summation of the last three terms in (60) is an augmented form of the cost function of the conventional LIKES algorithm (see [23] for more details), and hence mLIKES reduces to LIKES when there are no one-bit measurements. Note that $\ln |\mathbf{R}|$ is a concave function of \mathbf{p} , σ_0^2 and $\frac{1}{\eta_1^2}$, and we use the majorization-minimization (MM) technique [16] to simply it to attain enhanced computational efficiency.

Given the estimates of \mathbf{p} , σ_0 , η_1 at the m -th MM iteration and $\hat{\mathbf{R}}^m$ constructed by (61), a majorizing function for $\ln |\mathbf{R}|$ can be easily constructed by its first-order Taylor expansion:

$$\ln |\mathbf{R}| \leq \sum_{k=1}^{K_\theta K_\omega} w_k p_k + \bar{w}_0 \sigma_0^2 + \frac{\bar{w}_1}{\eta_1^2}, \quad (63)$$

where

$$\begin{aligned} w_k &= \tilde{\mathbf{a}}_k^H (\hat{\mathbf{R}}^m)^{-1} \tilde{\mathbf{a}}_k, \quad k = 1, \dots, K_\theta K_\omega, \\ \bar{w}_0 &= \mathbf{1}_{NL}^T \tilde{\mathbf{p}} [\boldsymbol{\delta} \otimes \mathbf{1}_N], \\ \bar{w}_1 &= \mathbf{1}_{N(M_r-L)}^T \tilde{\mathbf{p}} [\tilde{\boldsymbol{\delta}} \otimes \mathbf{1}_N] \quad \text{with } \tilde{\mathbf{p}} = \text{diag}((\hat{\mathbf{R}}^m)^{-1}), \end{aligned} \quad (64)$$

with $\tilde{\mathbf{a}}_k$ being the k -th column of $\tilde{\mathbf{A}}$. Making use of (63), we can obtain a majorizing function for (60) at the $(m+1)$ -th

MM iteration as follows:

$$Q^{m+1}(\boldsymbol{\alpha}, \mathbf{p}, \sigma_0, \eta_1) = -\ln L_1(\boldsymbol{\alpha}, \eta_1) + \psi^{m+1}(\boldsymbol{\alpha}, \mathbf{p}, \sigma_0, \eta_1), \quad (65)$$

where

$$\begin{aligned} \psi^{m+1}(\boldsymbol{\alpha}, \mathbf{p}, \sigma_0, \eta_1) &\triangleq \frac{1}{\sigma_0^2} \|\mathbf{A}_0 \mathbf{b} - \mathbf{y}_0\|^2 + \sum_{k=1}^{K_\theta K_\omega} \frac{|\alpha_k|^2}{p_k} \\ &+ \sum_{k=1}^{K_\theta K_\omega} w_k p_k + \bar{w}_0 \sigma_0^2 + \frac{\bar{w}_1}{\eta_1^2}. \end{aligned} \quad (66)$$

The minimization of $Q^{m+1}(\boldsymbol{\alpha}, \mathbf{p}, \sigma_0, \eta_1)$ is still a highly nonlinear and non-convex optimization problem and hard to solve. To mitigate the difficulty, we again adopt the MM technique, referred to as the inner MM iteration, to iteratively minimize (65). Let $f(x) = -\ln \Phi(x)$. The analysis of $f(x)$ in [24] demonstrates that for all $x \in \mathbb{R}$, $f(x)$ has a bounded second-order derivative:

$$0 < f''(x) < 1. \quad (67)$$

The following inequality follows from the Lagrange's mean value theorem and the inequality in (67):

$$\frac{|f'(x) - f'(y)|}{|x - y|} = |f''(\xi)| < 1 \text{ for every } x, y \in \mathbb{R}, \quad (68)$$

where $x \leq \xi \leq y$. The inequality in (68) implies that $f(x)$ is a continuously differentiable function with Lipschitz constant equal to 1. Then, the following inequality holds for any $x, y \in \mathbb{R}$

$$\begin{aligned} f(x) &\leq f(y) + f'(y)(x - y) + \frac{1}{2}(x - y)^2 \\ &= \frac{1}{2} [x - (y - \nabla f(y))]^2 + \text{const.} \end{aligned} \quad (69)$$

Define $\boldsymbol{\gamma} = [\gamma(1), \dots, \gamma(N(M_r - L))]^T$ with

$$\begin{aligned} \gamma_R(n) &= y_{1,R} \sqrt{2} \eta_1 \Re[\mathbf{a}_{1,n} \boldsymbol{\alpha} - h_1(n)] \\ \gamma_I(n) &= y_{1,I} \sqrt{2} \eta_1 \Im[\mathbf{a}_{1,n} \boldsymbol{\alpha} - h_1(n)]. \end{aligned} \quad (70)$$

Using this notation, $-\ln L_1(\boldsymbol{\alpha}, \eta_1)$ can be rewritten as:

$$-\ln L_1(\boldsymbol{\alpha}, \eta_1) = \sum_{n=1}^{N(M_r - L)} f(\gamma_R(n)) + \sum_{n=1}^{N(M_r - L)} f(\gamma_I(n)). \quad (71)$$

Making use of (69), a majorizing function for $-\ln L_1(\boldsymbol{\alpha}, \eta_1)$ can be constructed as follows:

$$-\ln L_1(\boldsymbol{\alpha}, \eta_1) \leq \frac{1}{2} \|\boldsymbol{\gamma} - (\hat{\boldsymbol{\gamma}}_i^{m+1} - \nabla f(\hat{\boldsymbol{\gamma}}_i^{m+1}))\|^2 + \text{const}, \quad (72)$$

where $\hat{\boldsymbol{\gamma}}_{R/I,i}^{m+1}(n)$ is the estimate of $\gamma_{R/I}(n)$ at the i -th inner MM iteration performed at the $(m+1)$ -th outer MM iteration. Combined with $\psi(\boldsymbol{\alpha}, \mathbf{p}, \sigma_0, \eta_1)$, a majorizing function for $Q^{m+1}(\boldsymbol{\alpha}, \mathbf{p}, \sigma_0, \eta_1)$ at the $(i+1)$ -th iteration is given as follows:

$$\begin{aligned} Q^{m+1}(\boldsymbol{\alpha}, \mathbf{p}, \sigma_0, \eta_1) &\leq \frac{1}{2} \|\boldsymbol{\gamma} - (\hat{\boldsymbol{\gamma}}_i^{m+1} - \nabla f(\hat{\boldsymbol{\gamma}}_i^{m+1}))\|^2 \\ &+ \psi^{m+1}(\boldsymbol{\alpha}, \mathbf{p}, \sigma_0, \eta_1) + \text{const.} \end{aligned} \quad (73)$$

Inserting (70) into (73) leads to the minimization of the following optimization criterion:

$$\begin{aligned} \bar{\Psi}(\boldsymbol{\alpha}, \mathbf{p}, \sigma_0, \eta_1) &= \eta_1^2 \|\mathbf{A}_1 \boldsymbol{\alpha} - \mathbf{h}_1 - \frac{1}{\sqrt{2} \eta_1} \mathbf{g}_i^{m+1}\|^2 \\ &+ \psi^{m+1}(\boldsymbol{\alpha}, \mathbf{p}, \sigma_0, \eta_1). \end{aligned} \quad (74)$$

where $\mathbf{g}_i^{m+1} = [g_i^{m+1}(1), \dots, g_i^{m+1}(N(M_r - L))]^T$,

$$\begin{aligned} g_i^{m+1}(n) &= y_{1,R}(n) u_{R,i}^{m+1}(n) + j y_{1,I}(n) u_{I,i}^{m+1}(n), \\ u_{R/I,i}^{m+1}(n) &= \hat{\gamma}_{R/I,i}^{m+1}(n) - \nabla f(\hat{\gamma}_{R/I,i}^{m+1}(n)), \\ \hat{\gamma}_{R,i}^{m+1}(n) &= y_{1,R} \sqrt{2} \eta_i^{m+1} \Re[\mathbf{a}_{1,n}^T \hat{\boldsymbol{\alpha}}_i^{m+1} - h_1(n)], \end{aligned}$$

and

$$\hat{\gamma}_{I,i}^{m+1}(n) = y_{1,I} \sqrt{2} \eta_i^{m+1} \Im[\mathbf{a}_{1,n}^T \hat{\boldsymbol{\alpha}}_i^{m+1} - h_1(n)]. \quad (75)$$

The minimization of (74) can be achieved by using a blockwise cyclic algorithm, which alternately minimizes (74) with respect to $\boldsymbol{\alpha}, \mathbf{p}, \sigma_0$ and η_1 .

1) *Updating $\boldsymbol{\alpha}$* : Let

$$\bar{\mathbf{y}}_{1,i}^{m+1} = \mathbf{h}_1 + \frac{1}{\sqrt{2} \hat{\eta}_{1,i}^{m+1}} \mathbf{g}_i^{m+1}. \quad (76)$$

Ignoring the terms independent of $\boldsymbol{\alpha}$ yields the following iterative scheme:

$$\min_{\boldsymbol{\alpha}} (\hat{\eta}_{1,i}^{m+1})^2 \|\mathbf{A}_1 \boldsymbol{\alpha} - \bar{\mathbf{y}}_{1,i}^{m+1}\|^2 + \frac{\|\mathbf{A}_0 \mathbf{b} - \mathbf{y}_0\|^2}{(\hat{\sigma}_{0,i}^{m+1})^2} + \sum_{k=1}^{K_\theta K_\omega} \frac{|\alpha_k|^2}{\hat{p}_{k,i}^{m+1}}, \quad (77)$$

or equivalently,

$$\min_{\boldsymbol{\alpha}} (\bar{\mathbf{y}}_i^{m+1} - \bar{\mathbf{A}} \boldsymbol{\alpha})^H (\hat{\boldsymbol{\Sigma}}_i^{m+1})^{-1} (\bar{\mathbf{y}}_i^{m+1} - \bar{\mathbf{A}} \boldsymbol{\alpha}) + \sum_{k=1}^{K_f K_\theta} \frac{|\alpha_k|^2}{\hat{p}_{k,i}^{m+1}}, \quad (78)$$

where

$$\begin{aligned} \bar{\mathbf{y}}_i^{m+1} &= [\mathbf{y}_0^T \quad (\bar{\mathbf{y}}_{1,i}^{m+1})^T]^T \\ \hat{\boldsymbol{\Sigma}}_i^{m+1} &= \begin{bmatrix} (\hat{\sigma}_{0,i}^{m+1})^2 \mathbf{I}_{NL} & \mathbf{0} \\ \mathbf{0} & 1/(\hat{\eta}_{1,i}^{m+1})^2 \mathbf{I}_{N(M_r - L)} \end{bmatrix}. \end{aligned} \quad (79)$$

Lemma 3 in [23] indicates that minimizing (78) yields:

$$\hat{\boldsymbol{\alpha}}_{i+1}^{m+1} = \hat{\mathbf{P}}_i^{m+1} \bar{\mathbf{A}}^H (\hat{\mathbf{R}}_i^{m+1})^{-1} \bar{\mathbf{y}}_i^{m+1}, \quad (80)$$

and the minimum value is

$$(\bar{\mathbf{y}}_i^{m+1})^H (\hat{\mathbf{R}}_i^{m+1})^{-1} \bar{\mathbf{y}}_i^{m+1}. \quad (81)$$

2) *Updating \mathbf{p}* : To update \mathbf{p} at the $(i+1)$ -th MM iteration, we need to solve the following subproblem:

$$\hat{\mathbf{p}}_{i+1}^{m+1} = \arg \min_{\mathbf{p}} \sum_{k=1}^{K_\theta K_\omega} \frac{|\hat{\alpha}_{k,i+1}^{m+1}|^2}{p_k} + \sum_{k=1}^{K_\theta K_\omega} w_k p_k. \quad (82)$$

It is easy to check that the solution to the above optimization problem is:

$$\hat{p}_{k,i+1}^{m+1} = |\hat{\alpha}_{k,i+1}^{m+1}| / \sqrt{w_k}. \quad (83)$$

3) *Updating σ_0 and η_1* : Ignoring the terms independent of σ_0 yields the following subproblem:

$$\hat{\sigma}_{0,i+1}^{m+1} = \arg \min_{\sigma_0} \frac{1}{\sigma_0^2} \|\mathbf{A}_0 \hat{\boldsymbol{\alpha}}_{i+1}^{m+1} - \mathbf{y}_0\|^2 + \bar{w}_0 \sigma_0^2. \quad (84)$$

The solution to the above optimization problem is:

$$\hat{\sigma}_{0,i+1}^{m+1} = \frac{\sqrt{\|\mathbf{A}_0 \hat{\boldsymbol{\alpha}}_{i+1}^{m+1} - \mathbf{y}_0\|}}{\bar{w}_0^{1/4}}. \quad (85)$$

Similarly, we can update η_1 by solving the following subproblem:

$$\hat{\eta}_{1,i+1}^{m+1} = \arg \min_{\eta_1} \eta_1^2 \|\mathbf{A}_1 \hat{\boldsymbol{\alpha}}_{i+1}^{m+1} - \mathbf{h}_1 - \frac{1}{\sqrt{2}\eta_1} \mathbf{g}_i^{m+1}\|^2 + \frac{\bar{w}_1}{\eta_1^2}. \quad (86)$$

The optimization problem in (86) contains just one variable and is obviously convex with respect to η_1 . Therefore, the updating of η_1 can be efficiently implemented by minimizing the above objective function by using, for example, the MATLAB `fminbnd` function.

Note that the monotonicity property of the mLIKES algorithm is guaranteed since

$$\begin{aligned} \Psi(\hat{\boldsymbol{\alpha}}^m, \hat{\eta}_1^m, \hat{\sigma}_0^m, \hat{\mathbf{p}}^m) &= Q^{m+1}(\hat{\boldsymbol{\alpha}}^m, \hat{\eta}_1^m, \hat{\sigma}_0^m, \hat{\mathbf{p}}^m) \quad (87) \\ &\geq Q^{m+1}(\hat{\boldsymbol{\alpha}}^{m+1}, \hat{\eta}_1^{m+1}, \hat{\sigma}_0^{m+1}, \hat{\mathbf{p}}^{m+1}) \quad (88) \\ &\geq \Psi(\hat{\boldsymbol{\alpha}}^{m+1}, \hat{\eta}_1^{m+1}, \hat{\sigma}_0^{m+1}, \hat{\mathbf{p}}^{m+1}) \quad (89) \end{aligned}$$

Both the equality in (87) and the inequality in (89) follow from the property of the majorizing function. The inequality in (88) comes from the minimization of $Q^{m+1}(\boldsymbol{\alpha}, \eta_1, \sigma_0, \mathbf{p})$ by using the inner MM iterations. Therefore mLIKES is guaranteed a local convergence.

Remark 1: Observe from (73) that at the $(i+1)$ -th inner MM iteration, we approximate $Q^{m+1}(\boldsymbol{\alpha}, \mathbf{p}, \sigma_0, \eta_1)$ by replacing $-\ln L_1(\boldsymbol{\alpha}, \eta_1)$ with its linear approximation at $\hat{\gamma}_i^{m+1}$, which is also the basic idea of the proximal gradient descent algorithm [21, 25]. It was shown in [20, 21] that the Nesterov acceleration technique can speed up the proximal gradient descent to attain an optimal convergence rate. Herein we also adopt the idea of the Nesterov acceleration technique to accelerate the convergence rate of the inner MM iterations. Instead of approximating $-\ln L_1(\boldsymbol{\alpha}, \eta_1)$ at the point $\hat{\gamma}_i^{m+1}$, we can make the approximation at an extrapolated point $\tilde{\gamma}_i^{m+1}$, which linearly combines the two previous points $\{\hat{\gamma}_i^{m+1}, \hat{\gamma}_{i-1}^{m+1}\}$:

$$\tilde{\gamma}_i^{m+1} = \hat{\gamma}_{R/I,i}^{m+1} + \left(\frac{t_i - 1}{t_{i+1}}\right) (\hat{\gamma}_{R/I,i}^{m+1} - \hat{\gamma}_{R/I,i-1}^{m+1}), \quad (90)$$

with $t_{i+1} = \frac{1 + \sqrt{1 + 4t_i^2}}{2}$ and $t_0 = 1$. At the $(i+1)$ -th iteration, the optimization problem described in (73) can be replaced by the following counterpart:

$$\min_{\boldsymbol{\alpha}, \mathbf{p}, \sigma_0, \eta_1} \eta_1^2 \|\boldsymbol{\gamma} - (\tilde{\gamma}_i^{m+1} - \nabla f(\tilde{\gamma}_i^{m+1}))\|^2 + \psi^{m+1}(\boldsymbol{\alpha}, \mathbf{p}, \sigma_0, \eta_1) \quad (91)$$

It follows from (73) and (74) that (91) can be reformulated as:

$$\min_{\boldsymbol{\alpha}, \mathbf{p}, \sigma_0, \eta_1} \eta_1^2 \|\mathbf{A}_1 \boldsymbol{\alpha} - \mathbf{h}_1 - \frac{1}{\sqrt{2}\eta_1} \tilde{\mathbf{g}}_i^{m+1}\|^2 + \psi^{m+1}(\boldsymbol{\alpha}, \mathbf{p}, \sigma_0, \eta_1), \quad (92)$$

where

$$\tilde{\mathbf{g}}_i^{m+1} = \mathbf{g}_i^{m+1} + \frac{t_i - 1}{t_{i+1}} (\mathbf{g}_i^{m+1} - \mathbf{g}_{i-1}^{m+1}). \quad (93)$$

Note that the optimization problem in (92) has the same form as the one in (74) except that \mathbf{g}_i^{m+1} in (74) takes the form in (93). The updating formulas for $\{\boldsymbol{\alpha}, \mathbf{p}, \sigma_0, \eta_1\}$ have similar forms as those in (80), (83), (85) and (86).

We summarize the detailed steps of the proposed mLIKES in Algorithm 1, where Steps 8 – 13 correspond to the inner MM iterations. Our extensive numerical simulations show that the inner MM iterations can typically converge within a few (e.g., 3) iterations while the number of outer MM iterations exceeds 5.

Remark 3: Compared with the inner updating steps of the conventional LIKES for the high-precision data (see [23, 26] for details), we find that the term $\tilde{\mathbf{y}}_{1,i}^{m+1}$ can be interpreted as an estimate of the high-precision data \mathbf{y}_1 . In each inner MM iteration, mLIKES reconstructs an estimate (i.e., $\tilde{\mathbf{y}}_{1,i}^{m+1}$) of the high-precision received signal (i.e., \mathbf{y}_1) using the most recently updated estimates from the previous step. Together with using the high-precision measurements \mathbf{y}_0 , mLIKES updates the sparse vector $\boldsymbol{\alpha}$ and \mathbf{p} by using the same formulas as the LIKES algorithm for the high-precision counterpart (see [23]). In other words, by using the MM technique, the sparse parameter estimation problem for the mixed-ADC based model in (58) can be approximately and iteratively solved by making use of a high-precision model with the high-precision data $\tilde{\mathbf{y}}_i^{m+1}$ given by:

$$\tilde{\mathbf{y}}_i^{m+1} = \tilde{\mathbf{A}}\boldsymbol{\alpha} + \tilde{\mathbf{e}}, \quad (94)$$

where the mean and covariance matrix of the noise vector $\tilde{\mathbf{e}}$ are 0 and $\tilde{\boldsymbol{\Sigma}}_i^{m+1}$, respectively.

B. Cyclically Refine the mLIKES Parameter Estimates

We first normalize the mLIKES angle-Doppler estimate $\hat{\boldsymbol{\alpha}}$ by $\hat{\eta}_1$, i.e., we obtain $\hat{\boldsymbol{\alpha}}\hat{\eta}_1$. Denote $\boldsymbol{\chi}_k = [\theta_k, \omega_k, \beta_{R,k}, \beta_{I,k}]$ as the parameters of the k -th strongest target. The estimate of $\boldsymbol{\chi}_k$, i.e., $\hat{\boldsymbol{\chi}}_k$, can be determined from the k -th maximum peak of the normalized mLIKES angle-Doppler image. We use the Bayesian information criterion [27] (BIC) to determine the number of targets K . The cost function of BIC for the mixed-ADC output is given by:

$$\text{mBIC}(\check{K}) = -2 \ln L(\{\hat{\boldsymbol{\chi}}_k\}_{k=1}^{\check{K}}, \eta_1) + (6\check{K} + 1) \ln(M_r M_t N). \quad (95)$$

The estimate \hat{K} of the number of targets is determined as the integer that minimizes the mBIC cost function with respect to the assumed number of targets \check{K} . Let $\mathcal{P} = \{\hat{\boldsymbol{\chi}}_1, \dots, \hat{\boldsymbol{\chi}}_{\hat{K}}\}$. The angle-Doppler parameter set \mathcal{P} can be considered as the coarse estimates, which can be refined by Algorithm 2, where $\hat{\boldsymbol{\chi}}_k = \arg \min_{\boldsymbol{\chi}_k} -\ln L(\boldsymbol{\chi}_k | \{\hat{\boldsymbol{\chi}}_j\}_{j=1, j \neq k}^{\hat{K}}, \hat{\eta})$, with $-\ln L(\boldsymbol{\chi}_k | \{\hat{\boldsymbol{\chi}}_j\}_{j=1, j \neq k}^{\hat{K}}, \hat{\eta})$ given in Equation (55) with all but the k -th target parameters replaced with their estimates. This represents the parameter refinement of the k -th target while fixing the parameters of the other targets,

Algorithm 1: mLIKES

Input: The mixed-ADC measurements: \mathbf{Y} (or \mathbf{y}_0 and \mathbf{y}_1);
Thresholds adopted by one-bit ADC: \mathbf{h}_1 .

Procedure:

- 1: Initialize $\hat{\alpha}_0$, $\hat{\mathbf{p}}_0$, $\hat{\sigma}_{0,0}$ and $\hat{\eta}_{1,0}$; $m = 0$.
- 2: **repeat**
- 3: Update $\hat{\mathbf{R}}^m$ with $\hat{\mathbf{p}}^m$, $\hat{\sigma}_0^m$ and $\hat{\eta}_1^m$ using (61).
- 4: Compute $\{w_k\}_{k=1}^{K_\theta K_\omega}$, \bar{w}_0 and \bar{w}_1 using (64).
- 5: Compute \mathbf{g}_0^{m+1} using (75); $\tilde{\mathbf{g}}_0^{m+1} = \mathbf{g}_0^{m+1}$;
- 6: $\hat{\mathbf{R}}_0^{m+1} = \hat{\mathbf{R}}^m$; $i = 0$; $t_0 = 1$.
- 7: **repeat**
- 8: Update $\hat{\alpha}_{i+1}^{m+1}$ and $\hat{\mathbf{p}}_{i+1}^{m+1}$ using (80) and (83).
- 9: Update $\hat{\sigma}_{0,i+1}^{m+1}$ and $\hat{\eta}_{1,i+1}^{m+1}$ using (85) and (86).
- 10: Construct $\hat{\mathbf{R}}_{i+1}^{m+1}$ with $\hat{\mathbf{p}}_{i+1}^{m+1}$, $\hat{\sigma}_{0,i+1}^{m+1}$ and $\hat{\eta}_{1,i+1}^{m+1}$.
- 11: Compute \mathbf{g}_{i+1}^{m+1} with $\hat{\alpha}_{i+1}^{m+1}$ and $\hat{\eta}_{1,i+1}^{m+1}$.
- 12: $t_{i+1} = \frac{1 + \sqrt{1 + 4t_i^2}}{2}$
- 13: $\tilde{\mathbf{g}}_{i+1}^{m+1} = \mathbf{g}_{i+1}^{m+1} + \left(\frac{t_i - 1}{t_{i+1}}\right) \mathbf{g}_{i+1}^{m+1}$
- 14: $i = i + 1$
- 15: **until** practical convergence
- 16: $m = m + 1$
- 17: **until** practical convergence

Output: $\hat{\alpha}$, $\hat{\sigma}_0$ and $\hat{\eta}_1$.

e.g., $\{\hat{\chi}_j\}_{j=1, j \neq k}^{\hat{K}}$. The noise parameter estimate η is always updated along with χ_1 . This refinement can be performed by using the interior-point based bounded optimization method (e.g., “fmincon” of MATLAB) over the angular interval $\left[\hat{\theta}_k - \frac{90^\circ}{K_\theta}, \hat{\theta}_k + \frac{90^\circ}{K_\theta}\right]$ and the Doppler interval $\left[\hat{\omega}_k - \frac{\pi}{K_\omega}, \hat{\omega}_k + \frac{\pi}{K_\omega}\right]$ to find the estimate of χ_k that minimizes $-\ln L\left(\chi_k | \{\hat{\chi}_j\}_{j=1, j \neq k}^{\hat{K}}, \eta\right)$. Note in passing that the idea of this cyclic refinement operation is similar to the last step of the well-known RELAX algorithm [28, 29], and hence we refer to the two-step estimator that combines mLIKES and a variation of the last step of RELAX as mLIKES&RELAX.

C. Complexity Analysis

For the proposed mLIKES algorithm, the construction of $\hat{\mathbf{R}}_{m+1}^{i+1}$ and the computation of $(\hat{\mathbf{R}}_{m+1}^{i+1})^{-1}$ have complexities of $\mathcal{O}(N^2 M_r^2 K_\theta K_\omega)$ and $\mathcal{O}(N^3 M_r^3)$, respectively. The update of $\{w_k\}_{k=1}^{K_\theta K_\omega}$ in (64) has a complexity of $\mathcal{O}(N^2 M_r^2 K_\theta K_\omega)$. The update of α in (80) requires a complexity of $\mathcal{O}(NM_r K_\theta K_\omega + N^2 M_r^2)$ by first computing $(\hat{\mathbf{R}}_i^{m+1})^{-1} \tilde{\mathbf{y}}_i^{m+1}$. The computational burden for updating \mathbf{p} , σ_0 and σ_1 is marginal and can be neglected. Hence, the total computational complexity of mLIKES is on the order of $\mathcal{O}(I_1(N^2 M_r^2 K_\theta K_\omega + N^3 M_r^3))$, where I_1 denotes the iteration number. It is worth noting that the proposed mLIKES algorithm for the mixed-ADC systems has computational complexities similar to those of the conventional LIKES algorithm for high-precision systems. The following RELAX-based fine searches can be performed using the interior-point based bounded optimization method (e.g.,

“fmincon” of MATLAB), where the computational cost is proportional to $\mathcal{O}(\tilde{N}^{3.5})$, where \tilde{N} is the number of design variables in χ_k . Assume that it requires I_2 iterations for RELAX-based algorithm to converge. The total computational complexity of mLIKES&RELAX is on the order of $\mathcal{O}(I_1(N^2 M_r^2 K_\theta K_\omega + N^3 M_r^3) + I_2 \tilde{N}^{3.5})$.

Algorithm 2: Cyclically refine the parameters

Input: $\mathcal{P} = \{\hat{\chi}_1, \dots, \hat{\chi}_{\hat{K}}\}$: Coarse estimates of the parameters obtained from mLIKES

\hat{K} : Estimated target number

Procedure:1: **repeat**

2: $\hat{\chi}_1, \hat{\eta} = \arg \min_{\chi_1, \eta} -\ln L\left(\chi_1, \eta | \{\hat{\chi}_j\}_{j=2}^{\hat{K}}\right)$

3: **for** $k = 2, \dots, \hat{K}$

4: $\hat{\chi}_k = \arg \min_{\chi_k} -\ln L\left(\chi_k | \{\hat{\chi}_j\}_{j=1, j \neq k}^{\hat{K}}, \hat{\eta}\right)$

5: **end for**

6: **until** practical convergence

Output: $[\hat{\theta}_1, \hat{\omega}_k, \hat{b}_k = \hat{\beta}_k / \hat{\eta}]$ for $k = 1, \dots, \hat{K}$ and $\hat{\eta}$.

V. NUMERICAL EXAMPLES

In this section, we present several numerical examples to demonstrate the performance of the mixed-ADC based architecture and the proposed algorithms for PMCW MIMO radar angle-Doppler Imaging. The PMCW MIMO radar under consideration is equipped with $M_t = 10$ transmit antennas spaced at $d_t = 5\lambda$ and $M_r = 10$ receive antennas spaced at $d_r = \lambda/2$. With the filled receive array and sparse transmit array, we can effectively create a filled virtual array with 100 antennas, see (8). The slow-time sample number $N = 64$ PRI's are adopted to extract the Doppler information. Random binary sequences (i.e., $C(m, n) \in \{1, -1\}$ with equal probabilities) are used as the slow-time codes. All examples were run on a PC with Intel(R) Core(TM) i7-6700 CPU @ 3.40GHz and 64.0 GB RAM.

A. Cramér-Rao Bound for Mixed-ADC Based Receiver

For the mixed-ADC based architecture, we consider the following three situations²:

1. $\delta_1 = 1$ and $\{\delta_m = 0\}_{m=2}^{10}$, which means that the first receive antenna is equipped with a pair of high precision ADC's (i.e., for in-phase and quadrature (I/Q) branches) and all other receive antennas are equipped with one-bit (1b) ADC's;
2. $\delta_1 = 1$, $\delta_2 = 1$ and $\{\delta_m = 0\}_{m=3}^{10}$, which indicates that the first and second of the receive antennas are equipped with high-precision ADC's and the other 8 with one-bit ADC's;
3. $\{\delta_m = 1\}_{m=1}^5$ and $\{\delta_m = 0\}_{m=6}^{10}$.

²For a fixed L , our extensive numerical simulations demonstrate that the angle-Doppler estimation performance is not sensitive to the distribution of high-precision ADC's in a MIMO system.

We consider a case of $K = 2$ targets. First, we assume that, $\theta_1 = 22.5^\circ$, $\theta_2 = 25.3125^\circ$, $\omega_1 = 1.3$, $\omega_2 = 1.4$, $b_1 = 1e^{j\pi/4}$ and $b_2 = e^{j\pi/4}/r$. Therefore r represents the amplitude ratio between the strong and weak targets:

$$r = \frac{|b_1|}{|b_2|}. \quad (96)$$

We vary r from 1 to 1000. We also vary the noise variance to maintain the same $\text{SNR}_2 = 10$ dB for the weak target, for all values of r , where:

$$\text{SNR}_2 = 10 \log_{10} \frac{1}{r^2 \sigma^2} \text{dB}. \quad (97)$$

For the one-bit ADC system and the one-bit part of the mixed-ADC based architecture, the PRI-varying (slow-time varying) threshold has the real and imaginary parts selected randomly and equally likely from a predefined eight-element set $\{-h_{\max}, -h_{\max} + \Delta, \dots, h_{\max} - \Delta, h_{\max}\}$ with $h_{\max} = \sqrt{p_{\text{out}}}$ and $\Delta = h_{\max}/7$, where $\sqrt{p_{\text{out}}}$ is the average received signal power at the I/Q channels.

Figs. 2 and 3 show the root CRBs (RCRBs) for θ and ω (see the explanations in the figure captions). Note from Fig. 2 that the high-precision root CRBs for ω_1 and θ_1 , decrease with r because σ^2 decreases as r increases and hence SNR_1 increases with r . For the weak target, the high-precision root CRBs in Fig. 3 for ω_2 and θ_2 are constant as r varies because SNR_2 is the same for all values of r . Note that the high-precision sampling receiver does not suffer from dynamic range problems even when r is very large. For $r = 1000$ for example, the first target is 60 dB stronger than the second one.

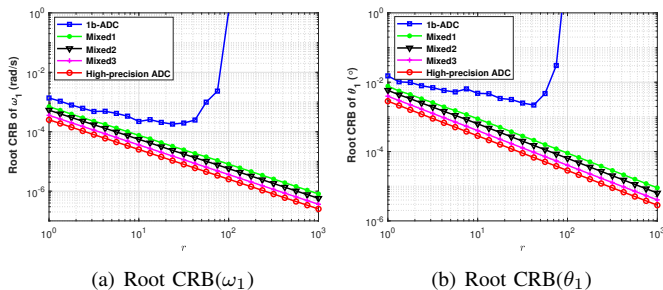


Fig. 2. Root CRB versus r for (a) ω_1 and (b) θ_1 .

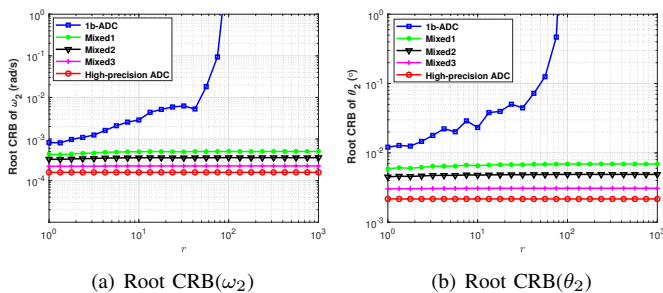


Fig. 3. Root CRB versus r for (a) ω_2 and (b) θ_2 .

The 1b-based CRB in Figs. 2 and 3 for ω_1 , ω_2 , θ_1 and θ_2 are the largest of all the cases considered. This is the price paid

for the low-cost of the binary quantizers, and the increases of the root CRB's are significant and can reach unacceptable levels. This is the so-called dynamic range problem of coarse quantizations. Compared with the one-bit system, mixed-ADC based architectures (Situations 1, 2 and 3 are denoted as "Mixed1", "Mixed2" and "Mixed3", respectively) with just one pair of high precision ADC's can attain significant performance improvements, especially for large values of r (e.g., $r \geq 10$). Most notably, the root CRB's of ω_2 and θ_2 remain almost constant as r increases, and hence the mixed-ADC based architecture can be a viable solution to solve the dynamic range problems of using coarse quantizers to reduce cost and power consumption of PMCW MIMO radar. We note that with just one pair of high-precision ADC's, the mixed-ADC based system can attain a dynamic range as high as 60 dB without suffering from significant accuracy problems. Therefore the mixed-ADC architecture with one pair of high-precision ADC's and a large number of one-bit ADC's is a low-cost solution for PMCW radar.

B. Angle-Doppler Imaging

Finally, we present several numerical examples to demonstrate the angle-Doppler imaging performance of the proposed algorithm for the mixed-ADC based PMCW MIMO radar system.

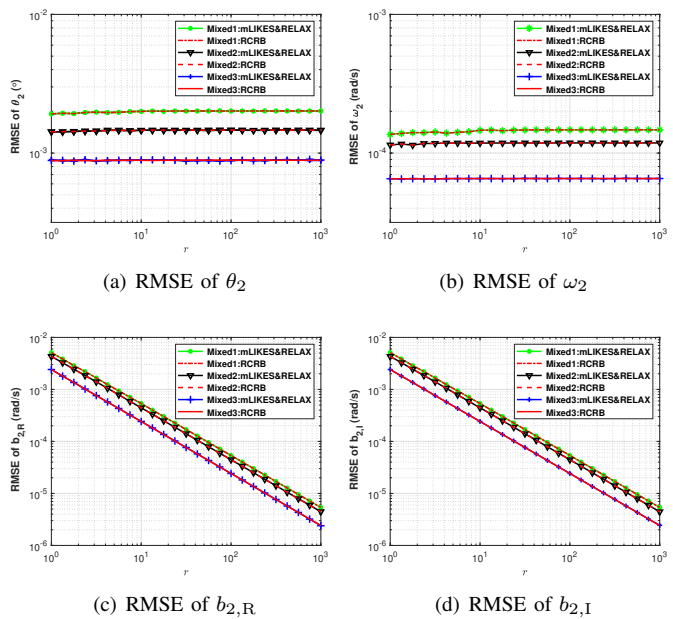


Fig. 4. Comparison between RCRBs and RMSEs of the parameter estimates of the second target as a function of r .

1) *Implementation details:* The number of grid points in the angular and Doppler domains are set to $K_\theta = 128$ and $K_\omega = 256$, respectively. In our simulations, the practical convergence of mLIKES is considered achieved when the relative change of \mathbf{p} between two consecutive iterations is below a small threshold. For the outer MM iterations, we use the threshold $\varepsilon_1 = 10^{-4}$ and we terminate the iterations when a maximum iteration number $I_1 = 50$ is reached. For the

inner MM iterations in mLIKES, we also set the threshold to $\varepsilon_2 = 10^{-4}$ and we terminate the iterations when a maximum iteration number $I_2 = 10$ is reached. For the RELAX-based cyclic refinement, we stop the iterations when the relative change of the negative log-likelihood function between two consecutive iterations is below 10^{-6} or a maximum iteration number reaching 50.

2) *Example 1:* Figs. 4(a)-4(d) show the root mean-squared errors (RMSEs) of the second target parameters obtained with 500 Monte-Carlo trials as a function of r . (The RMSEs of the first target parameter estimates obtained by using mLIKES&RELAX are close to the RCRB, and the plots are not shown herein.) It is observed from Fig. 4 that the RMSEs of the estimates obtained by using mLIKES&RELAX can approach the CRB for all values of r considered, i.e., for a dynamic range up to 60 dB.

3) *Example 2:* We now consider 30 moving targets with their angle-Doppler locations and powers indicated by the color-coded “○”, as shown in Fig. 5. Note that there are two off-grid targets marked with dash-dot rectangles. The amplitudes of the targets $\{|b_k|\}_{k=1}^{30}$ are selected randomly between 0.01 and 1, resulting in a dynamic range of 40 dB. The additive noise is assumed to be circularly symmetric i.i.d. complex-valued white Gaussian noise, with mean zero and a variance resulting in the minimum target SNR of 10 dB. Similar to Section V-A, the 8-level PRI-varying thresholds are considered for the one-bit system and the one-bit part of the mixed-ADC based architecture.

The angle-Doppler images obtained by using the matched filter with the high-precision data is shown in Fig. 5(a). Since the waveform orthogonality is not perfectly achieved in the Doppler domain, the slow-time code residuals are dispersed into the entire angle-Doppler images as pseudo noise. As a result, most weak targets are masked by the slow-time code residuals. However, we can observe from Fig. 5(b) that the LIKES algorithm can estimate the strong targets accurately and the weak targets reasonably well. In comparison, 1bLIKES misses quite a few weak targets, which is primarily due to the fact that the estimation performance offered by the one-bit quantizer degrades dramatically when the dynamic range of the signal components is high [14]. However, after introducing just one pair of high-precision ADC's, used at a single antenna output, into the one-bit ADC system, the dynamic range is drastically improved and mLIKES produces a satisfactory angle-Doppler image with all targets identified. Note from Figs. 5(b) and 5(d) that the two off-grid targets are slightly smeared. Fig. 5(e) shows that the cyclic refinement operation improves upon the mLIKES results and accurately determines the angle-Doppler locations of the two off-grid targets. The computational times needed by these methods in the present example are as follows: MF—0.02 seconds, LIKES—71 seconds, 1bLIKES—252 seconds, mLIKES—167 seconds, and mLIKES&RELAX—187 seconds.

VI. CONCLUSIONS

We have considered a mixed-ADC based architecture for PMCW MIMO radar systems. We have derived the CRB

for the system to characterize its best achievable unbiased estimation performance of target parameters. By making use of the MM technique, a computationally efficient estimator, referred to as mLIKES, has been introduced to obtain accurate angle-Doppler images. To further enhance the target parameter estimation performance, a RELAX-based approach is used to cyclically refine the mLIKES results to realize the ML estimation. Numerical examples have been presented to illustrate that the mixed-ADC based architecture with just one pair of high-precision ADC's at a single antenna output allows us to significantly reduce the hardware cost and power consumption while still maintain a high dynamic range needed by the automotive radar for autonomous driving applications. We have also demonstrated that the proposed algorithms can be used to attain good angle-Doppler imaging performances.

APPENDIX A

CRAMÉR-RAO BOUND FOR HIGH-PRECISION ADC'S

Note from [14][30] that the CRB formula for the data model in (5) is given by:

$$F(\varphi_i, \varphi_j) = \frac{2}{\sigma_0^2} \Re \left\{ \text{tr} \left[\frac{\partial(\mathbf{A}_r \mathbf{B} \mathbf{V}^T)^H}{\partial \varphi_i} \frac{\partial(\mathbf{A}_r \mathbf{B} \mathbf{V}^T)}{\partial \varphi_j} \right] \right\}. \quad (98)$$

The derivative of θ , ω , $\Re(\mathbf{b})$ and $\Im(\mathbf{b})$ with respect to $\mathbf{A}_r \mathbf{B} \mathbf{V}^T$ gives:

$$\begin{aligned} \frac{\partial(\mathbf{A}_r \mathbf{B} \mathbf{V}^T)}{\partial \theta_i} &= \dot{\mathbf{A}}_r \mathbf{e}_i \mathbf{e}_i^T \mathbf{B} \mathbf{V}^T + \mathbf{A}_r \mathbf{B} \mathbf{e}_i \mathbf{e}_i^T \dot{\mathbf{V}}_\theta^T, \\ \frac{\partial(\mathbf{A}_r \mathbf{B} \mathbf{V}^T)}{\partial \omega_i} &= \mathbf{A}_r \mathbf{B} \mathbf{e}_i \mathbf{e}_i^T \dot{\mathbf{V}}_\omega^T, \\ \frac{\partial(\mathbf{A}_r \mathbf{B} \mathbf{V}^T)}{\partial b_{R,i}} &= \mathbf{A}_r \mathbf{e}_i \mathbf{e}_i^T \mathbf{V}^T, \\ \frac{\partial(\mathbf{A}_r \mathbf{B} \mathbf{V}^T)}{\partial b_{I,i}} &= j \mathbf{A}_r \mathbf{e}_i \mathbf{e}_i^T \mathbf{V}^T, \end{aligned} \quad (99)$$

where $\dot{\mathbf{A}}_r$, $\dot{\mathbf{V}}_\theta$ and $\dot{\mathbf{V}}_\omega$ are defined in (27)–(29), respectively. Then

$$\begin{aligned} F(\theta_i, \theta_j) &= \frac{2}{\sigma_0^2} \Re \left\{ \text{tr} \left[(\dot{\mathbf{A}}_r \mathbf{e}_i \mathbf{e}_i^T \mathbf{B} \mathbf{V}^T + \mathbf{A}_r \mathbf{B} \mathbf{e}_i \mathbf{e}_i^T \dot{\mathbf{V}}_\theta^T)^H \right. \right. \\ &\quad \left. \left. \times (\dot{\mathbf{A}}_r \mathbf{e}_j \mathbf{e}_j^T \mathbf{B} \mathbf{V}^T + \mathbf{A}_r \mathbf{B} \mathbf{e}_j \mathbf{e}_j^T \dot{\mathbf{V}}_\theta^T) \right] \right\}. \end{aligned} \quad (100)$$

Next note that

$$\begin{aligned} &\text{tr} \left[(\dot{\mathbf{A}}_r \mathbf{e}_i \mathbf{e}_i^T \mathbf{B} \mathbf{V}^T)^H (\dot{\mathbf{A}}_r \mathbf{e}_j \mathbf{e}_j^T \mathbf{B} \mathbf{V}^T) \right] \\ &= (\mathbf{e}_i^T \dot{\mathbf{A}}_r \dot{\mathbf{A}}_r \mathbf{e}_j) (\mathbf{e}_j^T \mathbf{B}^* \mathbf{V}^* \mathbf{V}^T \mathbf{B} \mathbf{e}_i) \\ &= (\dot{\mathbf{A}}_r \dot{\mathbf{A}}_r)_{i,j} (\mathbf{B}^* \mathbf{V}^H \mathbf{V} \mathbf{B})_{i,j}, \end{aligned} \quad (101)$$

where we have used the fact that $\text{tr}(\mathbf{ABC}) = \text{tr}(\mathbf{BCA})$. The other three matrix product terms in (100) have similar forms, and hence \mathbf{F}_{11} has the form in (21). Similar to the derivation of \mathbf{F}_{11} , the other sub-matrices of the FIM follow immediately and are given in (22)–(26).

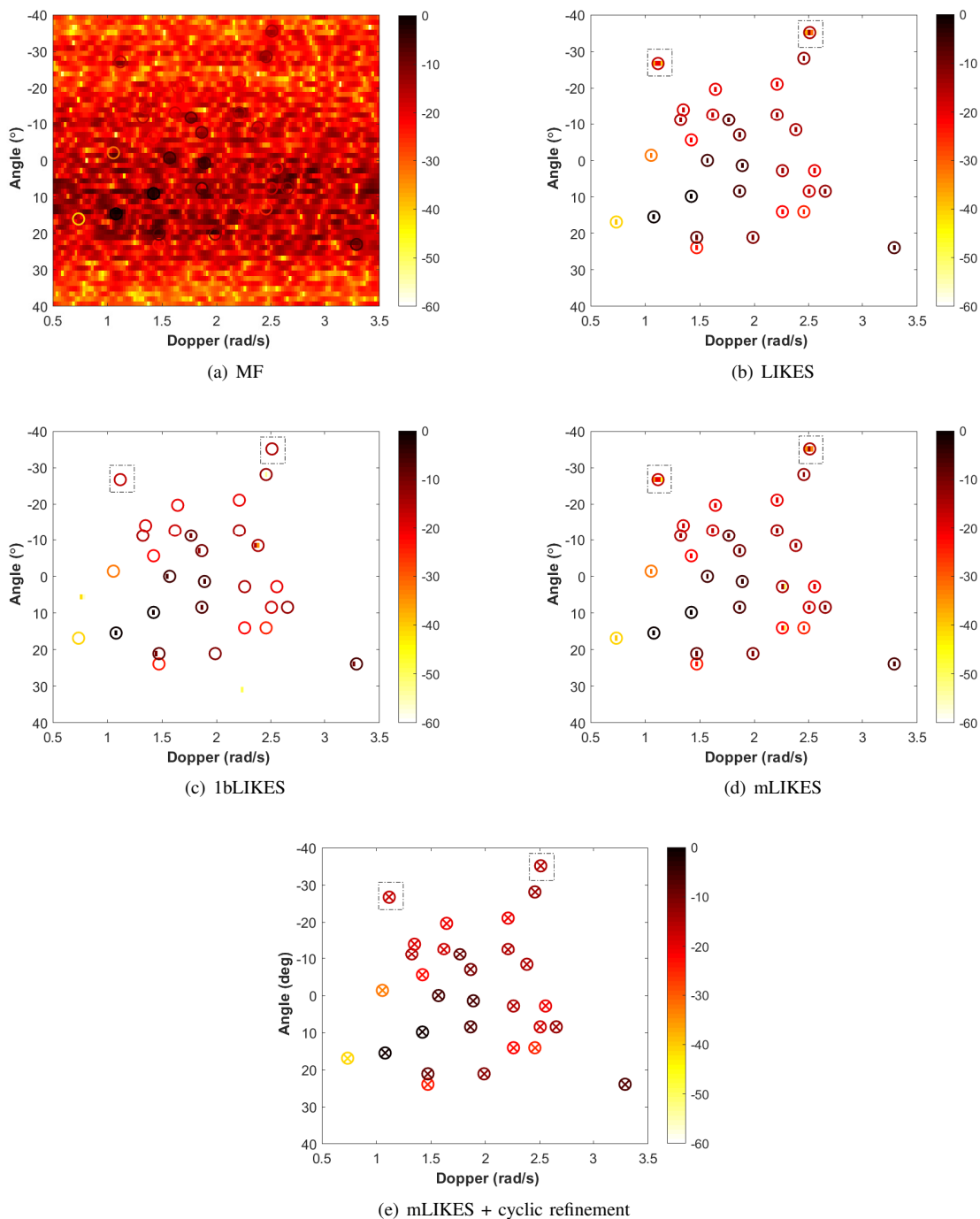


Fig. 5. Angle-Doppler images of mixed-ADC based PMCW MIMO radar, obtained by applying (a) matched filter, (b) LIKES to the high-precision data, (c) 1bLIKES to the one-bit data and (d) mLIKES and (e) mLIKES&RELAX to the Mixed1 outputs. “○” symbols indicate the locations of the true targets (color-coded according to power, in dB). All power levels are in dB. The dash-dot rectangles in (b)-(e) indicate the off-grid targets. “X” symbols in Fig. 5(e) represent targets estimated by mLIKES&RELAX.

REFERENCES

- [1] S. Sun, A. P. Petropulu, and H. V. Poor, "MIMO radar for advanced driver-assistance systems and autonomous driving: Advantages and challenges," *IEEE Signal Process. Mag.*, vol. 37, no. 4, pp. 98–117, 2020.
- [2] D. Bliss and K. Forsythe, "Multiple-input multiple-output (MIMO) radar and imaging: Degrees of freedom and resolution," in *Proc. 37th Asilomar Conf. Signals, Syst. Comput.*, Pacific Grove, USA, Nov. 2003.
- [3] J. Li and P. Stoica, "MIMO radar with colocated antennas," *IEEE Signal Process. Mag.*, vol. 24, no. 5, pp. 106–114, 2007.
- [4] —, *MIMO radar signal processing*. Wiley, 2009.
- [5] S. Alland, W. Stark, M. Ali, and M. Hegde, "Interference in automotive radar systems: Characteristics, mitigation techniques, and current and future research," *IEEE Signal Process. Mag.*, vol. 36, no. 5, pp. 45–59, 2019.
- [6] A. Banerjee, K. Vaesen, A. Visweswaran, K. Khalaf, Q. Shi, S. Brebels, D. Guermandi, C.-H. Tsai, J. Nguyen, A. Medra *et al.*, "Millimeter-wave transceivers for wireless communication, radar, and sensing," in *Proc. IEEE Custom Integr. Circuits Conf. (CICC)*, Austin, TX, USA, Apr. 2019.
- [7] R. H. Walden, "Analog-to-digital converter survey and analysis," *IEEE J. Sel. Areas Commun.*, vol. 17, no. 4, pp. 539–550, 1999.
- [8] Y. Cheng, X. Shang, J. Li, and P. Stoica, "Interval design for signal parameter estimation from quantized data," *IEEE Trans. Signal Process.*, vol. 70, pp. 6011–6020, 2022.
- [9] O. Bar-Shalom and A. J. Weiss, "DOA estimation using one-bit quantized measurements," *IEEE Trans. Aerosp. Electron. Syst.*, vol. 38, no. 3, pp. 868–884, 2002.
- [10] J. Fang, Y. Shen, H. Li, and Z. Ren, "Sparse signal recovery from one-bit quantized data: An iterative reweighted algorithm," *Signal Process.*, vol. 102, pp. 201–206, 2014.
- [11] B. Zhao, L. Huang, and W. Bao, "One-bit SAR imaging based on single-frequency thresholds," *IEEE Trans. Geosci. Remote Sens.*, vol. 57, no. 9, pp. 7017–7032, 2019.
- [12] X. Shang, J. Li, and P. Stoica, "Weighted SPICE algorithms for range-Doppler imaging using one-bit automotive radar," *IEEE J. Sel. Topics in Signal Process.*, vol. 15, no. 4, pp. 1041–1054, 2021.
- [13] C.-Y. Wu, T. Zhang, J. Li, and T. F. Wong, "Parameter estimation in PMCW MIMO radar systems with few-bit quantized observations," *IEEE Trans. Signal Process.*, vol. 70, no. 10, pp. 810–821, 2022.
- [14] P. Stoica, X. Shang, and Y. Cheng, "The Cramér-Rao bound for signal parameter estimation from quantized data [Lecture Notes]," *IEEE Signal Process. Mag.*, vol. 39, no. 1, pp. 118–125, 2021.
- [15] D. R. Hunter and K. Lange, "A tutorial on MM algorithms," *The American Statistician*, vol. 58, no. 1, pp. 30–37, 2004.
- [16] P. Stoica and Y. Selen, "Cyclic minimizers, majorization techniques, and the expectation-maximization algorithm: A refresher," *IEEE Signal Process. Mag.*, vol. 21, no. 1, pp. 112–114, 2004.
- [17] J. Mairal, "Incremental majorization-minimization optimization with application to large-scale machine learning," *SIAM J. Optim.*, vol. 25, no. 2, pp. 829–855, 2015.
- [18] M. Hong, M. Razaviyayn, Z.-Q. Luo, and J.-S. Pang, "A unified algorithmic framework for block-structured optimization involving big data: With applications in machine learning and signal processing," *IEEE Signal Process. Mag.*, vol. 33, no. 1, pp. 57–77, 2015.
- [19] Y. Sun, P. Babu, and D. P. Palomar, "Majorization-minimization algorithms in signal processing, communications, and machine learning," *IEEE Trans. Signal Process.*, vol. 65, no. 3, pp. 794–816, 2016.
- [20] Y. E. Nesterov, "A method for solving the convex programming problem with convergence rate $O(1/k^2)$," in *Dokl. Akad. Nauk SSSR*, vol. 269, 1983, pp. 543–547.
- [21] A. Beck and M. Teboulle, "A fast iterative shrinkage-thresholding algorithm for linear inverse problems," *SIAM J. Imaging Sci.*, vol. 2, no. 1, pp. 183–202, 2009.
- [22] C. Li, R. Zhang, J. Li, and P. Stoica, "Bayesian information criterion for signed measurements with application to sinusoidal signals," *IEEE Signal Process. Lett.*, vol. 25, no. 8, pp. 1251–1255, 2018.
- [23] P. Stoica, D. Zachariah, and J. Li, "Weighted SPICE: A unifying approach for hyperparameter-free sparse estimation," *Digital Signal Processing*, vol. 33, pp. 1–12, 2014.
- [24] J. Ren, T. Zhang, J. Li, and P. Stoica, "Sinusoidal parameter estimation from signed measurements via majorization–minimization based RELAX," *IEEE Trans. Signal Process.*, vol. 67, no. 8, pp. 2173–2186, 2019.
- [25] L. M. Bregman, "The relaxation method of finding the common point of convex sets and its application to the solution of problems in convex programming," *USSR Computational Mathematics and Mathematical Physics*, vol. 7, no. 3, pp. 200–217, 1967.
- [26] P. Stoica and P. Babu, "SPICE and LIKES: Two hyperparameter-free methods for sparse-parameter estimation," *Signal Process.*, vol. 92, no. 7, pp. 1580–1590, 2012.
- [27] P. Stoica and Y. Selen, "Model-order selection: A review of information criterion rules," *IEEE Signal Process. Mag.*, vol. 21, no. 4, pp. 36–47, 2004.
- [28] J. Li and P. Stoica, "Efficient mixed-spectrum estimation with applications to target feature extraction," *IEEE Trans. signal process.*, vol. 44, no. 2, pp. 281–295, 1996.
- [29] J. Li, D. Zheng, and P. Stoica, "Angle and waveform estimation via RELAX," *IEEE Trans. Aerosp. Electron. Syst.*, vol. 33, no. 3, pp. 1077–1087, 1997.
- [30] J. Li, L. Xu, P. Stoica, K. W. Forsythe, and D. W. Bliss, "Range compression and waveform optimization for MIMO radar: A Cramér–Rao bound based study," *IEEE Trans. Signal Process.*, vol. 56, no. 1, pp. 218–232, 2007.